



Investigation of the energy-extraction regime of a novel semi-passive flapping-foil turbine concept with a prescribed heave motion and a passive pitch motion

Matthieu Boudreau^{a,1}, Kevin Gunther^a, Guy Dumas^{a,2}.

^aCFD Laboratory LMFN, Département de génie mécanique, Université Laval, Québec, QC, Canada, G1V 0A6

Postprint, 2019 - Journal of Fluids and Structures

Published version available online at: <https://doi.org/10.1016/j.jfluidstructs.2018.11.014>

Abstract

Due to the inherent complexity of the mechanisms needed to prescribe the heave and the pitch motions of optimal flapping-foil turbines, several research groups are now investigating the potential of using unconstrained motions. The amplitude, the phase and the frequency of such passive motions are resulting from the interaction of the foil with the flow and its elastic supports, namely springs and dampers. More specifically, this work proposes an innovative semi-passive flapping-foil turbine concept with a prescribed sinusoidal heave motion and a passive pitch motion. Two-dimensional numerical simulations have been carried out at a Reynolds number of 3.9×10^6 based on the chord length with a foil having its pitch axis located at the quarter-chord point. A parametric study has been conducted by varying the value of the static moment, which involves the distance between the center of mass and the pitch axis, and the frequency of the prescribed heave motion. Different responses of the foil have been observed and one of them corresponds to an energy-extraction regime that is characterized by periodic limit-cycle oscillations of large amplitudes with a phase lag between the heave and the pitch motions ranging between 90° and 105° . A maximum efficiency of 45.4% has been reached, hence confirming the great potential of this turbine concept. This work shows that such good performance is achieved when the center of mass of the foil is located downstream of the pitch axis and when no leading-edge vortices are formed.

Keywords: Oscillating foil, Power generation, Fluid-structure interaction, Leading-edge vortex

1. Introduction

1.1. Context

By constraining a foil to undergo combined heave (translational) and pitch (rotational) motions with adequate kinematics, it is possible to extract a significant amount of energy from a fluid flow (Young et al., 2014; Xiao and Zhu, 2014). This concept is known as the flapping-foil turbine and it has primarily been developed with the objective of using it as a hydrokinetic turbine to extract energy from rivers or tidal currents. Efficiencies exceeding 40% have been obtained when prescribing appropriate heave and pitch motions (Kinsey and Dumas, 2014), which results in what we refer to as a fully-constrained flapping-foil turbine. However, prescribing these motions presents several challenges regarding the design of such a device. Indeed, the mechanisms that are used to achieve the desired foil motions are complex, which can affect the costs and the reliability of the apparatus. Furthermore, the complexity of these mechanisms can also result in significant power losses due to the friction occurring in the large number of moving components involved, as reported by Kinsey et al. (2011).

An alternative consisting in a device for which only the pitch motion is prescribed has been proposed (Abiru and Yoshitake, 2011, 2012; Chen et al., 2018; Deng et al., 2015; Derakhshandeh et al., 2016; Griffith et al., 2016; Huxham et al., 2012; Shimizu et al., 2008; Sitorus et al., 2015; Teng et al., 2016; Wu et al., 2014, 2015; Zhan et al., 2017; Zhu et al., 2009; Zhu and Peng, 2009). The heave motion is then said to be passive as the foil is elastically supported with springs and dampers for this degree of freedom instead of being connected to the turbine structure with rigid links.

¹matthieu.boudreau.1@ulaval.ca

²gdumas@gmc.ulaval.ca

As a result, the heave motion cannot be prescribed and rather results from the interaction of the pitching foil with its elastic supports and the flow. The use of this simplified turbine concept, known in the literature as the semi-passive flapping-foil turbine, allows getting rid of the complex coupling mechanisms linking both degrees of freedom that are needed in the case of the fully-constrained concept. Efficiencies exceeding 30% were reported by Deng et al. (2015) and Teng et al. (2016), who carried out 2D unconfined numerical simulations, while Abiru and Yoshitake (2011, 2012) and Huxham et al. (2012) conducted experiments in water channels and measured efficiencies reaching 20%. Griffith et al. (2016) evaluated the energy-extraction potential of a device for which the foil was replaced by different elliptical cylinders having an aspect ratio ranging from 1 (circular cylinder) to 6. They showed that the amount of energy extracted is increasing as the aspect ratio of the elliptical cylinder is increased, hence suggesting that a foil geometry is optimal for this type of turbine and that turbines solely relying on the vortex-induced vibration phenomenon are less efficient. While this semi-passive flapping-foil turbine concept is simpler than its fully-constrained counterpart, it still requires an actuator and a controller in pitch in addition to an electric generator in heave, the latter being usually modeled as a viscous damper.

A simpler device for which both degrees of freedom are independent and elastically supported has also been proposed and is known as the fully-passive flapping-foil turbine concept (Peng and Zhu, 2009; Veilleux and Dumas, 2017; Zhu, 2012; Wang et al., 2017; Boudreau et al., 2018). Again, no coupling mechanism is needed with such a device but, unlike the semi-passive concept presented above, no actuator and no controller are required in pitch. A few numerical studies showed that different types of response can be observed by varying the values of the structural parameters governing the turbine dynamics and the flow characteristics (Peng and Zhu, 2009; Veilleux and Dumas, 2017; Wang et al., 2017). Among these different responses, only one is appropriate in an energy extraction perspective and it is characterized by large amplitudes and periodic heave and pitch motions. This regular response was also observed experimentally by Boudreau et al. (2018) using a fully-passive turbine prototype in a water channel. The sensitivity of the turbine performance to seven different parameters affecting the turbine dynamics was evaluated and a maximum efficiency of 31% was reported by the authors. While this performance has confirmed the potential of the fully-passive turbine concept, it does not match the best performance reported for the fully-constrained flapping-foil turbine yet.

The studies conducted on the fully-passive flapping-foil turbine have demonstrated that it is possible to achieve a good level of performance with a passive pitch motion. Since most of the energy extracted by flapping-foil turbines comes from the heave motion (Kinsey and Dumas, 2008, 2014; Zhu, 2011), it is logical to connect an electric generator to this degree of freedom, thereby allowing one to constrain this motion. Following this idea, the current work proposes a novel semi-passive flapping-foil turbine concept for which the heave motion is prescribed and the pitch motion is passive. This results in a simpler device than the other semi-passive turbine version described above since no actuator and no controller are required in pitch. The objective of this study consists in evaluating the potential of this innovative flapping-foil turbine concept compared to the other turbine designs that have already been proposed. Moreover, this work aims at developing a fundamental understanding of the dynamics of passive pitch motions, which is not only relevant for the semi-passive flapping-foil turbine proposed in this work, but also for the fully-passive flapping-foil turbine concept. This is achieved by varying the static moment, which is a structural parameter involving the distance between the center of mass and the pitch axis that has not received a lot of attention in the literature so far. Indeed, most of the studies conducted on semi-passive and fully-passive flapping-foil turbines either considered a pitch axis coinciding with the center of mass (Abiru and Yoshitake, 2011, 2012; Deng et al., 2015; Griffith et al., 2016; Shimizu et al., 2008; Teng et al., 2016; Wu et al., 2014, 2015; Zhan et al., 2017) or massless foils (Peng and Zhu, 2009; Zhu et al., 2009; Zhu and Peng, 2009; Zhu, 2012). Moreover, the present work is performed at a large Reynolds number of 3.9×10^6 representative of full-scale turbines, unlike most of the previous studies on flapping-foil turbine which rather considered low Reynolds numbers of the order of 1 000 (Young et al., 2014; Xiao and Zhu, 2014).

More information about the use of passive or prescribed motions is given in Sec. 1.2. The semi-passive turbine concept considered in this study is described in Sec. 2.1. The fluid and solid solvers that are used, their validation and the definition of different performance metrics are presented in Secs. 2.2 to 2.5. A description of the different types of response that have been observed in this study is then given in Sec. 3.1 followed by an analysis of the role of the electric generator for this turbine concept in Sec. 3.2.

1.2. Additional information regarding the use of passive or prescribed motions

The motions undergone by the foil of a flapping-foil turbine can be characterized with 5 motion parameters, namely the motion shape and amplitude in heave, the motion shape and amplitude in pitch, the heave frequency, the pitch frequency and the phase lag between the heave and the pitch motions. Each of these motion parameters can be left free or constrained depending on the specific design of the flapping-foil turbine.

We refer to as a fully-constrained turbine when all the motion parameters are constrained. This can be achieved by using three components: 1) a slider-crank linkage to convert the reciprocating heave motion to a rotating motion and to connect the foil to an electric generator, hence constraining the motion shape and amplitude in heave; 2) a controller to enforce a constant rotational velocity of the electric generator's rotor, which imposes the frequency of the heave motion; 3) rigid links to mechanically couple both degrees of freedom together, thereby also constraining the motion shape and amplitude and pitch, the frequency of the pitch motion and the phase lag between both degrees of freedom. One example of such a fully-constrained turbine prototype is described in the work of Kinsey et al. (2011).

Another possibility is to leave all the motion parameters free to obtain what we refer to as a fully-passive turbine. This has been done by Peng and Zhu (2009), Veilleux and Dumas (2017), Wang et al. (2017) and Boudreau et al. (2018). Such a turbine concept is obtained when no slider-crank linkage, no coupling mechanism and no controller are used. Nevertheless, springs and dampers can be independently connected to the foil in heave and in pitch to allow an indirect control of the motions. Moreover, such turbine is designed to restrict the motions to the heave and pitch degrees of freedom only.

Several other "semi-passive" alternatives are possible between these two extreme cases by constraining or not each of the five motion parameters describing the flapping-foil motions. The most popular semi-passive concept in the literature involves a passive heave motion and a prescribed pitch motion (Abiru and Yoshitake, 2011, 2012; Chen et al., 2018; Deng et al., 2015; Derakhshandeh et al., 2016; Griffith et al., 2016; Huxham et al., 2012; Shimizu et al., 2008; Sitorus et al., 2015; Teng et al., 2016; Wu et al., 2014, 2015; Zhan et al., 2017; Zhu et al., 2009; Zhu and Peng, 2009). More specifically, an actuator and a controller allow constraining the motion shape and amplitude in pitch in addition to the frequency of this motion while letting all the other motion parameters free because the foil of such a device is elastically supported in heave. Young et al. (2013) have proposed another turbine concept for which a slider-crank linkage and a coupling mechanism are present but no controller is used. As a result, all the motion parameters are constrained except the frequency, which is however constrained to be the same for both degrees of freedom due to the presence of the coupling mechanism. It is worth mentioning that they have used the term fully-passive to describe this turbine concept in their study, but their definition is different from the one proposed in the current work. Indeed, we define a fully-passive turbine as one for which all the motion parameters are free.

As mentioned earlier, a novel semi-passive turbine concept with a prescribed heave motion and a passive pitch motion is proposed in this study. More specifically, this implies that the foil is elastically supported with springs and dampers in pitch and that a slider-crank linkage is required to convert the reciprocating heave motion to a rotating motion, hence constraining the motion shape and amplitude in heave. This slider-crank linkage also connects the foil to an electrical generator, which is controlled to enforce a constant rotational velocity and thus, a constrained frequency for the heave motion. However, no coupling mechanism is used, therefore leaving all the remaining motion parameters, namely the motion shape and amplitude in pitch, the frequency of the pitch motion and the phase lag between the heave and the pitch motions, free. For the sake of conciseness, we use the term semi-passive turbine to refer to this heave-prescribed semi-passive turbine concept in this work. This should not be confused with other semi-passive turbine concepts that have been studied in the literature.

2. Methodology

2.1. Turbine description

The semi-passive flapping-foil turbine considered in this study, which is shown schematically in Fig. 1, consists in a rigid NACA0015 foil that is elastically-supported in pitch (θ) with a prescribed heave motion (h). The pitch motion is entirely governed by the following equation of motion:

$$M = I_{\theta} \ddot{\theta} + S \dot{h} \cos(\theta) + D_{\theta} \dot{\theta} + k_{\theta} \theta, \quad (1)$$

where the superscript (\cdot) denotes a time derivative, M is the moment about the pitch axis resulting from the fluid loading, I_θ is the moment of inertia about the pitch axis, S is the static moment, which corresponds to the pitching mass (m_θ) times the distance between the center of mass and the pitch axis (x_θ) (see Fig. 1 for the sign convention):

$$S = m_\theta x_\theta , \quad (2)$$

D_θ is the pitch damping coefficient and k_θ is the pitch spring stiffness coefficient (rotational stiffness). Note that the static moment is zero when the pitch axis coincides with the center of mass and that the gravitational acceleration does not appear in the equation of motion because it is considered to act in a direction aligned with the pitch axis (z -direction in Fig. 1).

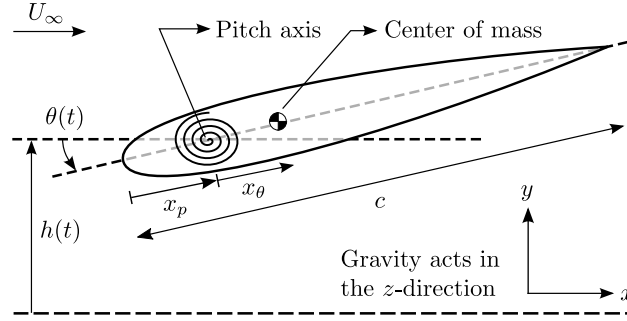


Figure 1: Outline of the semi-passive flapping-foil turbine concept with a prescribed heave motion and a passive pitch motion. Note that x_θ is defined positive as shown in the figure, namely with the center of mass being located downstream of the pitch axis.

In its dimensionless form, Eq. 1 becomes:

$$C_M/2 = I_\theta^* \ddot{\theta}^* + S^* \ddot{h}^* \cos(\theta) + D_\theta^* \dot{\theta}^* + k_\theta^* \theta , \quad (3)$$

with:

$$C_M = \frac{M}{0.5 \rho U_\infty^2 b c^2} , \quad I_\theta^* = \frac{I_\theta}{\rho b c^4} , \quad S^* = \frac{S}{\rho b c^3} , \quad D_\theta^* = \frac{D_\theta}{\rho U_\infty b c^3} , \quad k_\theta^* = \frac{k_\theta}{\rho U_\infty^2 b c^2} ,$$

$$h^* = \frac{h}{c} , \quad \dot{h}^* = \frac{\dot{h}}{U_\infty} , \quad \ddot{h}^* = \frac{\ddot{h} c}{U_\infty^2} , \quad \dot{\theta}^* = \frac{\dot{\theta} c}{U_\infty} , \quad \ddot{\theta}^* = \frac{\ddot{\theta} c^2}{U_\infty^2} ,$$

where ρ is the fluid density, U_∞ is the freestream velocity, c is the chord length and b is the span length. Note that forces per unit span are always considered in this work, so that b is taken to be unity ($b = 1$).

The heave motion is prescribed to be a sine wave with an amplitude growing linearly from zero to its nominal value (H_0) over the first three foil oscillations:

$$h = H_0 \min\left(\frac{t}{3T}, 1\right) \sin(2\pi f t) , \quad (4)$$

where t is time, f is the frequency of the prescribed heave motion and T is the period of one oscillation or cycle ($T = 1/f$). This linear growth of the heave amplitude at the beginning of the simulations is used in order to avoid imposing a shock in heave velocity or heave acceleration, therefore providing a smooth initial condition.

Throughout the current study, the dimensionless heave amplitude (H_0/c), the dimensionless moment of inertia (I_θ^*), and the dimensionless pitch damping coefficient (D_θ^*) are all kept constant with the values listed in Table 1. A heave amplitude of one chord length has been chosen based on the study of the fully-constrained concept conducted by Kinsey and Dumas (2014) and because the best efficiencies reported in the works of Veilleux and Dumas (2017), Wang et al. (2017) and Boudreau et al. (2018) on fully-passive flapping-foil turbines have been obtained with a passive heave motion having an amplitude of that order ($1c$). The dimensionless moment of inertia is set to 2, which is similar

to the mass ratio used in the work of Wang et al. (2017) on a fully-passive turbine. An idealized turbine with no friction in pitch is considered. As a result, the pitch damping coefficient is set to zero. This is justified by the fact that the pitch damping should be minimized in practice since it results in undesired losses of energy. As a reference point, the pitch damping coefficient was of the order of $D_\theta^* = 0.005$ for the fully-passive flapping-foil turbine prototype tested by Boudreau et al. (2018). For all the cases considered in this study, the pitch axis is located at the quarter-chord point ($x_p/c = 0.25$) and the dimensionless pitch spring stiffness coefficient (k_θ^*) is set so that the dimensionless pitch natural frequency always matches the reduced frequency of the prescribed heave motion. This results in:

$$k_\theta^* = (2\pi f^*)^2 I_\theta^* , \quad (5)$$

where f^* is given by:

$$f^* = f c / U_\infty . \quad (6)$$

The Reynolds number is fixed at 3.9×10^6 , based on the chord length, in order to characterize large-scale turbines (e.g., Cape Sharp Tidal Venture Ltd. (2018)). It also ensures that the boundary layers are turbulent, which allows us to solve them with a turbulence model in fully turbulent mode, as stated in Sec. 2.2. The results of the present study are expected to be representative of turbines operating at different Reynolds numbers provided that they are large enough so that the boundary layers remain turbulent. Moreover, this choice is consistent with previous works conducted on large-scale hydrokinetic turbines (e.g., Boudreau and Dumas (2017); Sitorus and Ko (2019)). The values of the dimensionless static moment (S^*) and the reduced frequency of the prescribed heave motion (f^*) are respectively varied between 0 and 0.8 and between 0.10 and 0.30. These ranges have been selected based on preliminary results and previous studies conducted on fully-constrained flapping-foil turbines (Kinsey and Dumas, 2014; Young et al., 2014; Xiao and Zhu, 2014).

Table 1: Governing parameter values

Parameter	Value
$\text{Re} = U_\infty c / \nu$	3.9×10^6
x_p/c	0.25
H_0/c	1
I_θ^*	2
D_θ^*	0
k_θ^*	$(2\pi f^*)^2 I_\theta^*$
S^*	0 to 0.8
f^*	0.10 to 0.30

2.2. Fluid and solid solvers

The semi-passive turbine concept proposed in this work is analyzed by carrying out two-dimensional incompressible Unsteady Reynolds-Averaged Navier-Stokes (URANS) simulations using the Spalart-Allmaras one-equation turbulence model with rotation correction (Dacles-Mariani et al., 1995, 1999; Spalart and Allmaras, 1994). Kinsey and Dumas (2012) and Veilleux and Dumas (2017) have previously validated the use of this turbulence modeling approach for the study of flapping-foil turbines by comparing their numerical results with experimental data. Siemens' STAR-CCM+® software is used as the fluid solver with second-order numerical schemes and a segregated approach making use of the SIMPLE algorithm for the pressure-velocity coupling (Ferziger and Perić, 2002). The computational domain is the same as the one used in the work of Veilleux and Dumas (2017) and it simply consists in a square of

100 chord lengths by 100 chord lengths with the foil being located at the center. A uniform and constant velocity together with a modified turbulent viscosity ratio of three ($\tilde{\nu}/\nu = 3$) is imposed at the inlet boundary. The modified turbulent viscosity ($\tilde{\nu}$) is the variable of interest in the single equation of the Spalart-Allmaras turbulence model and it is related to the turbulent viscosity (ν_t) through an empirical relation (Spalart et al., 1997). An inlet value of three for the modified turbulent viscosity ratio has been chosen to ensure that the turbulence model is used in its fully turbulent mode, following the recommendation of Spalart and Rumsey (2007). At the outlet, a pressure of zero is imposed and symmetry conditions are used for the two remaining boundaries. Regarding the initial condition, the velocity and turbulent viscosity ratio values at the inlet along with the pressure value at the outlet are imposed throughout the computational domain.

The overset mesh technique is used to handle the foil motions with two different meshes, one for the background region and one for the foil region. A structured mesh is used near the foil surface with a dimensionless normal wall distance (y^+) of the order of one, a maximum growth factor of 1.2 and approximately 500 nodes around the foil. The background mesh region is composed of hexagonal cells for a total of about 78 614 cells. The time step corresponds to 0.003 convective time units for all the simulations:

$$\frac{\Delta t U_\infty}{c} = 0.003 . \quad (7)$$

This results in a number of time steps per foil oscillation ranging between approximately 1 100 and 3 300 depending on the frequency of the prescribed heave motion.

In order to solve Eq. 1, it is discretized in time and written as:

$$R_\theta^n = I_\theta \ddot{\theta}^n + S \ddot{h}^n \cos(\theta^n) + D_\theta \dot{\theta}^n + k_\theta \theta^n - M^n , \quad (8)$$

where:

$$\ddot{\theta}^n = c_1 \dot{\theta}^n + c_2 \dot{\theta}^{n-1} + c_3 \dot{\theta}^{n-2} , \quad (9)$$

$$\dot{\theta}^n = c_1 \theta^n + c_2 \theta^{n-1} + c_3 \theta^{n-2} , \quad (10)$$

$$\ddot{h}^n = c_1 \dot{h}^n + c_2 \dot{h}^{n-1} + c_3 \dot{h}^{n-2} , \quad (11)$$

$$\dot{h}^n = c_1 h^n + c_2 h^{n-1} + c_3 h^{n-2} , \quad (12)$$

R_θ is the residual of the discretized version of Eq. 1, the superscript n denotes the current time step to be solved, while $n - 1$ and $n - 2$ correspond to the two previous time steps, and c_1 , c_2 and c_3 are the constants of the numerical scheme. In the current study, the temporal discretization of the solid solver is chosen to match that of the fluid solver, namely a second-order backward difference scheme. This results in:

$$c_1 = \frac{3}{2 \Delta t} , \quad c_2 = \frac{-4}{2 \Delta t} , \quad c_3 = \frac{1}{2 \Delta t} , \quad (13)$$

where Δt is the time step.

Considering Eqs. 8 to 13, the only unknowns on the right hand side of Eq. 8 are θ^n and M^n since the heave motion is prescribed. However, these two unknowns are not independent as the hydrodynamic moment (M) is a function of the foil motion and thus of the pitch angle (θ). The objective therefore consists in finding the value of θ^n which minimizes the absolute value of the residual R_θ^n . In other words, the solver has to find the roots of the function on the right hand side of Eq. 8 with θ^n as the independent variable. It achieves this task with the secant method. The resulting fluid-solid coupling algorithm is written in pseudocode in Appendix A.

The formulation of the fluid-solid coupling algorithm is implicit since the value of the residual for the current time step (R_θ^n) is a function of both the pitch angle and the hydrodynamic moment at the same time step (θ^n and M^n). Consequently, the pitch angle is determined for a given time step by iterating and updating its value a few times within this specific time step. These iterations are referred to as outer loops in Appendix A and they are indicated with subscripts. For each outer loop, the fluid solver has to perform a few iterations with the updated pitch angle in order

to determine the moment (M_i^n) corresponding to the i^{th} outer loop. Fluid iterations are conducted until the difference between the moment coefficient (C_M) values obtained from two successive iterations falls below 10^{-5} . Outer loops are conducted until the difference between the pitch angle values in radians, estimated from the two last outer loops and normalized with $\pi/2$, falls below a given convergence criterion (ϵ), which is set to 10^{-8} . Three or four outer loops are typically required to reach convergence for the pitch angle. Once this is achieved, some additional fluid iterations are carried out to ensure that the fluid residuals for the pressure, the streamwise and transverse momentums and the turbulent viscosity at least drop by a factor of 10^{-4} for the first three residuals and 5×10^{-4} for the residual of the turbulent viscosity for a given time step. When the pitch angle and the fluid residuals' convergence criteria are all met, the time step is incremented and the process starts over.

2.3. Power transfer and performance metrics

In order to evaluate the power extracted by the semi-passive turbine investigated in the current work, it is useful to write a general equation of motion in heave:

$$F_y = m_h \ddot{h} + S (\ddot{\theta} \cos \theta - \dot{\theta}^2 \sin \theta) + D_h \dot{h} + F_{\text{gen}} , \quad (14)$$

where F_y is the component of the hydrodynamic force acting on the foil in the heave direction, m_h is the mass of the components undergoing the heave motion, D_h is the heave damping coefficient, which accounts for the possible presence of friction in heave, and F_{gen} corresponds to the force stemming from the presence of an electric generator.

Eq. 14 should not be confused with Eq. 4. Indeed, Eq. 14 is not solved during the simulations since the heave motion is rather prescribed according to Eq. 4. Nevertheless, Eq. 14 tells us that in order to prescribe a sinusoidal heave motion, the generator must be controlled and might have to act as an actuator during a fraction of the foil oscillations. In other words, on a real turbine setup, F_{gen} would need to be adjusted in real time so that the solution of Eq. 14 corresponds to the desired (imposed) heave motion given by Eq. 4.

The amount of power available at the generator is obtained by multiplying Eq. 14 with the heave velocity (\dot{h}). After putting all the terms on the left hand side of this equation, except F_{gen} , normalizing and cycle-averaging the result, one obtains the following relation for the different power coefficients:

$$\langle C_{P_h} \rangle + \langle C_{P_{m_h}} \rangle + \langle C_{P_{S,h}} \rangle + \langle C_{P_{D_h}} \rangle = \langle C_{P_{\text{gen}}} \rangle , \quad (15)$$

where the angle brackets indicate the cycle-averaging process and $\langle C_{P_{\text{gen}}} \rangle$ is the power coefficient available at the electric generator. Note that unless otherwise indicated, the term power coefficient refers to a cycle-averaged value.

A similar procedure is used for the pitch motion by multiplying Eq. 1 with the pitch velocity ($\dot{\theta}$). Again, after putting all the terms on the left hand side of the equation, normalizing and cycle-averaging the result, the following relation is obtained:

$$\langle C_{P_\theta} \rangle + \langle C_{P_{I_\theta}} \rangle + \langle C_{P_{S,\theta}} \rangle + \langle C_{P_{D_\theta}} \rangle + \langle C_{P_{k_\theta}} \rangle = 0 . \quad (16)$$

The different power coefficients appearing in Eqs. 15 and 16 are defined as:

$$\langle C_{P_h} \rangle = \frac{1}{T} \int_{t_i}^{t_i+T} \left(\frac{F_y \dot{h}}{0.5 \rho U_\infty^3 b c} \right) dt , \quad (17)$$

$$\langle C_{P_{m_h}} \rangle = \frac{1}{T} \int_{t_i}^{t_i+T} \left(\frac{-m_h \ddot{h} \dot{h}}{0.5 \rho U_\infty^3 b c} \right) dt , \quad (18)$$

$$\langle C_{P_{S,h}} \rangle = \frac{1}{T} \int_{t_i}^{t_i+T} \left(\frac{-S \dot{h} (\ddot{\theta} \cos \theta - \dot{\theta}^2 \sin \theta)}{0.5 \rho U_\infty^3 b c} \right) dt , \quad (19)$$

$$\langle C_{P_{D_h}} \rangle = \frac{1}{T} \int_{t_i}^{t_i+T} \left(\frac{-D_h \dot{h}^2}{0.5 \rho U_\infty^3 b c} \right) dt , \quad (20)$$

$$\langle C_{P_{\text{gen}}} \rangle = \frac{1}{T} \int_{t_i}^{t_i+T} \left(\frac{F_{\text{gen}} \dot{h}}{0.5 \rho U_{\infty}^3 b c} \right) dt, \quad (21)$$

$$\langle C_{P_{\theta}} \rangle = \frac{1}{T} \int_{t_i}^{t_i+T} \left(\frac{M \dot{\theta}}{0.5 \rho U_{\infty}^3 b c} \right) dt, \quad (22)$$

$$\langle C_{P_{I_{\theta}}} \rangle = \frac{1}{T} \int_{t_i}^{t_i+T} \left(\frac{-I_{\theta} \ddot{\theta} \dot{\theta}}{0.5 \rho U_{\infty}^3 b c} \right) dt, \quad (23)$$

$$\langle C_{P_{S,\theta}} \rangle = \frac{1}{T} \int_{t_i}^{t_i+T} \left(\frac{-S \dot{h} \dot{\theta} \cos(\theta)}{0.5 \rho U_{\infty}^3 b c} \right) dt, \quad (24)$$

$$\langle C_{P_{D_{\theta}}} \rangle = \frac{1}{T} \int_{t_i}^{t_i+T} \left(\frac{-D_{\theta} \dot{\theta}^2}{0.5 \rho U_{\infty}^3 b c} \right) dt, \quad (25)$$

$$\langle C_{P_{k_{\theta}}} \rangle = \frac{1}{T} \int_{t_i}^{t_i+T} \left(\frac{-k_{\theta} \theta \dot{\theta}}{0.5 \rho U_{\infty}^3 b c} \right) dt, \quad (26)$$

where t_i is the time at which a given cycle starts, which is defined as the moment at which $h = 0$ and $\dot{h} > 0$, and T is the period of one cycle ($T = 1/f$). The metrics $\langle C_{P_h} \rangle$ and $\langle C_{P_{\theta}} \rangle$ are the heave and pitch power coefficients and they measure the power transfers occurring between the foil and the flow. They are positive when the power is transferred from the flow to the foil. Conversely, a negative value for one of these power coefficient means that some power is required to maintain the corresponding motion. $\langle C_{P_{m_h}} \rangle$, $\langle C_{P_{I_{\theta}}} \rangle$ and $\langle C_{P_{k_{\theta}}} \rangle$ correspond to power transfers occurring between the foil motions and different forms of potential energy. $\langle C_{P_{D_h}} \rangle$ and $\langle C_{P_{D_{\theta}}} \rangle$ are necessarily negative and correspond to power losses due to the presence of friction in heave and in pitch. Finally, $\langle C_{P_{S,h}} \rangle$ and $\langle C_{P_{S,\theta}} \rangle$ stand for the power transfers occurring between the heave motion and the pitch motion through the inertial coupling terms in Eqs. 1 and 14, namely the terms involving the static moment. They are defined positive when they correspond to a power input in their respective equation (Eq. 15 or Eq. 16) and negative for a power output. For example, when $\langle C_{P_{S,h}} \rangle$ is negative but $\langle C_{P_{S,\theta}} \rangle$ is positive, some power is transferred from the heave motion to the pitch motion on a cycle-averaged basis³. They are equal to zero when the center of mass coincides with the pitch axis (see Eq. 2 and Fig. 1).

Throughout the current investigation, no friction is considered in heave and in pitch. Consequently, $D_h = 0$ and $D_{\theta} = 0$, and thus $\langle C_{P_{D_h}} \rangle = 0$ and $\langle C_{P_{D_{\theta}}} \rangle = 0$. Furthermore, when the foil motions are periodic, $\langle C_{P_{m_h}} \rangle$, $\langle C_{P_{I_{\theta}}} \rangle$ and $\langle C_{P_{k_{\theta}}} \rangle$ vanish because these terms are conservative (Veilleux, 2014). This is always true in the case of $\langle C_{P_{m_h}} \rangle$ since sinusoidal heave motions are prescribed. Under such conditions, Eqs. 15 and 16 simplify to:

$$\langle C_{P_h} \rangle + \langle C_{P_{S,h}} \rangle = \langle C_{P_{\text{gen}}} \rangle, \quad (27)$$

$$\langle C_{P_{\theta}} \rangle + \langle C_{P_{S,\theta}} \rangle = 0. \quad (28)$$

Also, $\langle C_{P_{S,h}} \rangle$ and $\langle C_{P_{S,\theta}} \rangle$ are equal but opposite when the motions are periodic:

$$\langle C_{P_{S,h}} \rangle = -\langle C_{P_{S,\theta}} \rangle. \quad (29)$$

By combining Eqs. 27 to 29, one finally obtains:

$$\langle C_{P_{\text{gen}}} \rangle = \langle C_{P_h} \rangle + \langle C_{P_{\theta}} \rangle. \quad (30)$$

³Note that these definitions are slightly different than those presented in the paper of Veilleux and Dumas (2017) due to a different sign convention used for θ .

This last relation means that when the foil motions are periodic and no friction is considered, the power coefficient at the generator is simply equal to the sum of the heave and pitch contributions of the power transferred between the foil and the flow. In other words, all the power extracted from the flow is available at the electric generator. Nevertheless, $\langle C_{P_{\text{gen}}} \rangle$ has been evaluated using Eq. 27 throughout this study to include the possibility of non-periodic pitch motions.

The results presented in this work are analyzed in terms of different performance metrics. Indeed, each foil oscillation or cycle can be characterized by its efficiency:

$$\eta = \langle C_{P_{\text{gen}}} \rangle c/d, \quad (31)$$

its pitch amplitude:

$$\Theta_0 = \frac{\theta_{\text{max}} - \theta_{\text{min}}}{2}, \quad (32)$$

and its phase lag between the heave and the pitch motions, here given in degrees:

$$\phi = \frac{360}{T} (t_{\theta_{\text{max}}} - t_{h_{\text{max}}}), \quad (33)$$

where d is the overall extent of the foil motion, i.e., the distance between the maximum and minimum positions reached by any point on the foil surface in the heave direction during this specific cycle, θ_{max} and θ_{min} are the maximum and minimum pitch angles reached during this same cycle and $t_{\theta_{\text{max}}}$ and $t_{h_{\text{max}}}$ are the instants at which the maximum pitch angle and the maximum heave position are attained. In addition to these metrics, the streamwise and heave force coefficients are defined as:

$$C_{F_x} = \frac{F_x}{0.5 \rho U_{\infty}^2 b c}, \quad (34)$$

$$C_{F_y} = \frac{F_y}{0.5 \rho U_{\infty}^2 b c}, \quad (35)$$

where F_x and F_y are the streamwise and transverse (heave) components of the hydrodynamic force acting on the foil.

The time-averaged values presented in this work have been determined by starting the averaging process after reaching limit-cycle oscillations (LCO) in order to avoid the transient period at the beginning of the simulations. A sufficient number of cycles have been completed in order to obtain converged values while also making sure that a minimum of 10 cycles has been used. For example, the time-averaged power coefficient at the generator is computed as:

$$\overline{C_{P_{\text{gen}}}} = \frac{1}{N_{\text{end}} - N_{\text{start}} + 1} \sum_{j=N_{\text{start}}}^{N_{\text{end}}} \langle C_{P_{\text{gen}}} \rangle_j, \quad (36)$$

where the subscript j stands for the j^{th} cycle, N_{start} is the cycle at which the averaging process begins, N_{end} is the total number of completed cycles and $\langle C_{P_{\text{gen}}} \rangle_j$ is the power coefficient at the generator for the j^{th} cycle.

2.4. Spatial and temporal resolution levels

In order to validate that the spatial and temporal resolution levels used to conduct the present study are adequate, simulations with two other resolution levels have been carried out. More specifically, both the time step and the spatial resolution of the mesh have been varied by 33%, while keeping a dimensionless normal wall distance (y^+) of the order of one at the foil surface, to obtain a fine resolution case and a coarse resolution case. This results in 42 697, 78 614 and 135 789 cells for the coarse mesh, the baseline mesh and the fine mesh, respectively. The time evolution of the pitch angle as a function of time is presented in Fig. 2 for the three resolution levels at an operating point characterized by $f^* = 0.20$ and $S^* = 0.65$. As will be discussed in Section 3.1.1, this operating point corresponds to the best efficiency point. Fig. 2 shows that the differences between the cases with the three resolution levels are negligible since the three curves are almost perfectly superimposed on each other. This therefore confirms that the baseline resolution is adequate.

In order to make sure that the time step is also adequate for cases with a large reduced frequency, some simulations have been conducted with time steps varying from 0.00225 to 0.01 convective time units for a case with $f^* = 0.30$ and $S^* = 0.5$. The time-averaged pitch amplitude and phase lag values obtained with the different time steps are presented

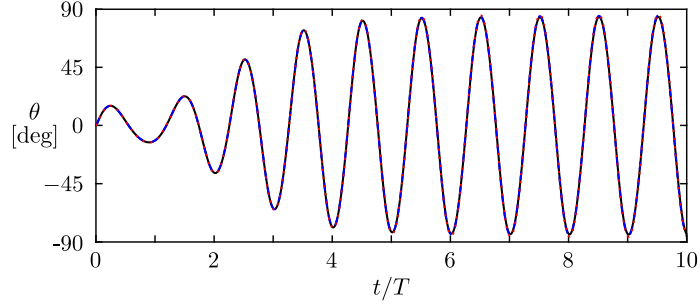


Figure 2: Time evolution of the pitch angle as a function of time during the first ten oscillations of an operating point characterized by $f^* = 0.20$ and $S^* = 0.65$ obtained with three different spatial and temporal resolution levels: coarse (dashed blue line), baseline (solid black line) and fine (dotted red line).

in Table 2. The maximum relative differences obtained between the different pitch amplitude and phase lag values are both around 1%. Moreover, the agreement between the time evolutions of the pitch angle obtained with the different time steps is as good as in Fig. 2. This confirms that the time step value of 0.003 convective time units that has been chosen to conduct this study is appropriate.

Table 2: Time-averaged pitch amplitude and phase lag values obtained with different temporal resolutions and the baseline mesh. These values are obtained from an operating point characterized by $f^* = 0.30$ and $S^* = 0.5$.

Time step ($\Delta t U_\infty / c$)	$\overline{\Theta}_0$	$\overline{\phi}$
0.01	85.3°	104.8°
0.006	84.8°	104.3°
0.004	84.8°	104.3°
0.003	84.8°	104.2°
0.00225	85.8°	105.2°

2.5. Validation

Some simulations of an elastically-supported cylinder undergoing vortex-induced vibrations (VIV) with various spring stiffness coefficients have been conducted to validate our numerical methodology. The benchmark case that has been chosen to perform this task was studied by Shiels et al. (2001), who used a viscous vortex method as the fluid solver. It consists in a massless cylinder of diameter D with no damping at a Reynolds number of 100. The equation of motion of such an elastically-supported cylinder is given by:

$$F_y = k y, \quad (37)$$

where F_y is the hydrodynamic force component normal to the freestream flow, y is the transverse displacement of the cylinder and k is the spring stiffness coefficient. This benchmark case has been chosen because such applications with large fluid-to-solid density ratios are known to be challenging for fluid-solid coupling algorithms.

As shown in Fig. 3, the results obtained with the present methodology are in good agreement with the results of Shiels et al. (2001). This confirms that our approach is not only accurate, but also stable and not limited in terms of the inertial property of the rigid body involved in the fluid-solid interaction problem to be solved.

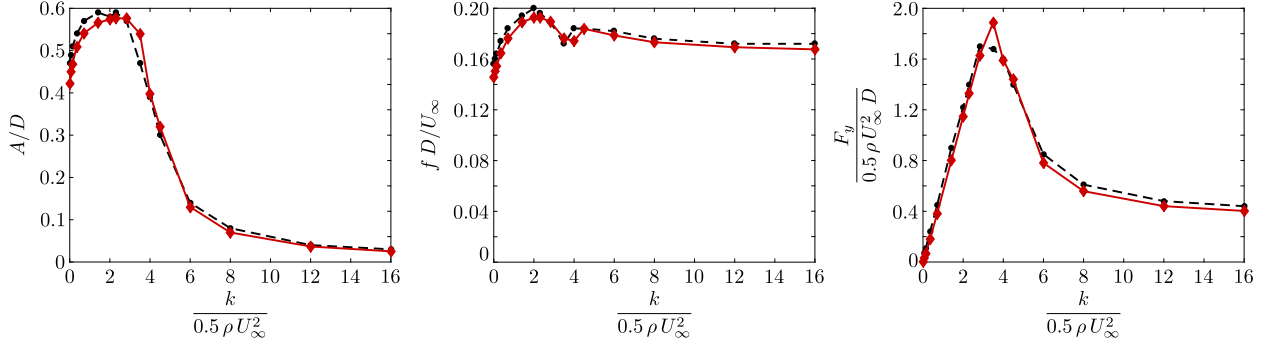


Figure 3: Comparison between the benchmark results of Shiels et al. (2001) (dashed black curves) and the results obtained with the present methodology (solid red curves) for a massless cylinder undergoing vortex-induced vibrations. The results are compared in terms of the amplitude of motion (A), the frequency of the motion (f) and the amplitude of the force component acting on the cylinder in the transverse direction (F_y).

Furthermore, our methodology has also been used to simulate the optimal fully-passive flapping-foil turbine case that was obtained by Veilleux and Dumas (2017) with their well-validated fluid-solid solver. The time evolutions of the heave position and the pitch angle obtained with our methodology are compared to their results in Fig. 4. It is found that our results agree well with those of Veilleux and Dumas (2017), hence confirming that our numerical methodology is suitable for fluid-solid simulations involving a flapping foil.

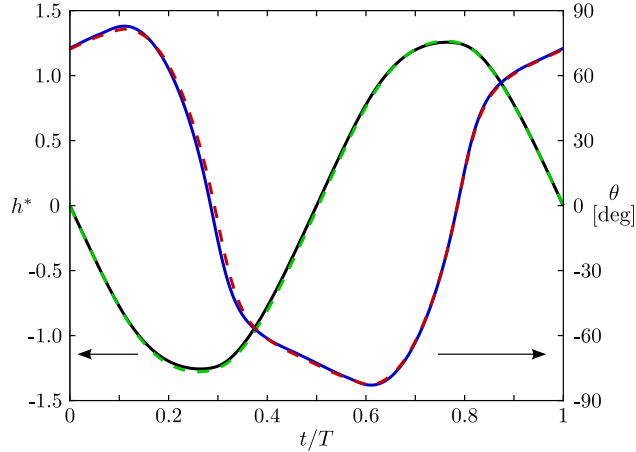


Figure 4: Comparison between the motions of a fully-passive flapping-foil turbine over one cycle of period T simulated with our numerical methodology (dashed lines) and as reported by Veilleux and Dumas (2017) (solid lines) for their optimal case. The dimensionless heave position (h^*) is shown in black and green while the pitch angle (θ) is shown in blue and red.

3. Results

3.1. Classification of the different regimes of motion

As mentioned in Sec. 2, the values of the dimensionless static moment (S^*) and the reduced frequency of the prescribed heave motion (f^*) are varied while all the other governing parameters are kept constant. Different responses are observed and they are classified into five different regimes of motion based on their time-averaged efficiency ($\bar{\eta}$), pitch amplitude ($\bar{\Theta}_0$) and phase lag ($\bar{\phi}$) values as well as the regularity of the motions. These regimes are represented with different colors and markers in Fig. 5, with each marker corresponding to a different simulated operating point.

Typical time evolutions of the pitch angle for each regime are shown in Fig. 6 while the contours of the time-averaged efficiency, the time-averaged pitch amplitude and the time-averaged phase lag between the heave and the

pitch motions are respectively presented in Figs. 7, 8a and 8b. The white areas in Fig. 7 indicate a negative efficiency. Also, the time-averaged values are not presented for the orange regime because of the irregularity of the response (see Fig. 6d). The corresponding regions in these figures are colored in gray. Note that we are not interested in the details of the orange regime since it is not suitable for a turbine application, as will be discussed below.

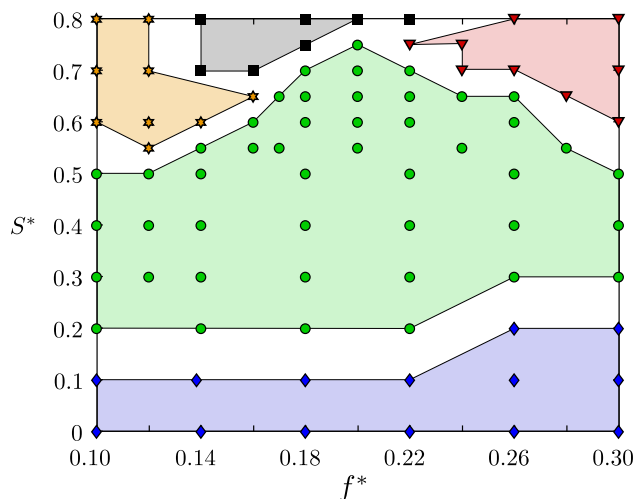


Figure 5: Classification of 5 different regimes of motion observed in the parametric space. Each marker corresponds to one simulated operating point.

The green regime contains the operating points characterized by periodic limit-cycle oscillations, and a positive energy extraction from the flow on a time-averaged basis, as seen in Fig. 7. This therefore makes it the only regime that is suitable for a turbine application. The motions in the blue regime rather require energy because it corresponds to a propulsion regime. The three other regimes, namely the black, the orange and the red regimes, correspond to neither energy-extraction regimes nor propulsion regimes. Unlike the periodic motions characterizing the green and the blue regimes, the motions characterizing these three other regimes are less regular (see Fig. 6) and they result in significant variations of the efficiency, the pitch amplitude and the phase lag from cycles to cycles. In fact, the efficiency of the operating points in these regimes can even alternate between positive and negative values. These large variations of the energy extraction occurring from cycles to cycles prevent these operating points from being potential candidates for a turbine application. Moreover, the time-averaged efficiency of these operating points is negative, except for a few exceptions for which the time-averaged efficiency nevertheless remains small.

As observed in Fig. 8b, the different regimes of motion are characterized by time-averaged phase lags ($\bar{\phi}$) around 90° , above 90° and below 90° . When the phase lag is larger than 90° , the leading edge points outward when the maximum and minimum heave positions are reached. In other words, a negative pitch angle is observed when the maximum heave position is reached, and vice versa. The opposite behavior is observed when the phase lag is smaller than 90° . This is shown schematically in Fig. 9 and it can also be observed in Fig. 10, which presents the limit-cycle oscillations of typical operating points in three different regimes characterized with different time-averaged phase lag values.

Even though our main interest in this investigation is directed toward the energy-extraction regime (green regime), the four other regimes are also described in the following sections in order to better highlight the distinctive features of the energy-extraction regime. Lastly, note that for all the operating points considered in this study, the dominant frequency component of the passive pitch motion is always synchronized with the frequency of the prescribed heave motion. The symbol f^* therefore refers to the frequency of both motions.

3.1.1. Green regime (energy extraction)

As already mentioned, the pitch amplitude is almost constant from cycles to cycles in the green regime (operating points denoted with green dots), except during the initial transient period. It is worth recalling that the pitch motion

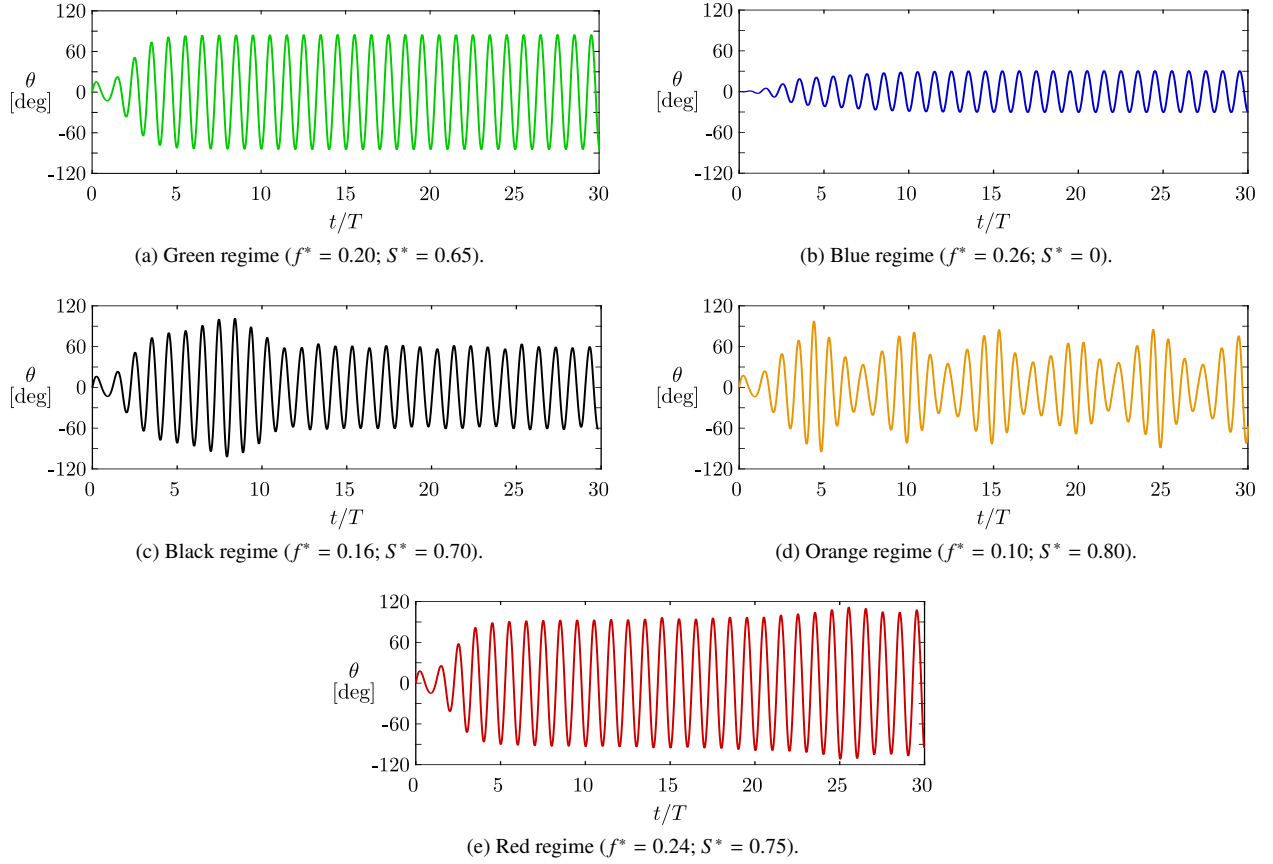


Figure 6: Typical time evolutions of the passive pitch motion as a function of time during the 30 first cycles for each regime of motion. Note that more than 30 cycles have been simulated and that the operating point in the red regime has only reached a permanent response after completing 52 cycles.

is not prescribed and it rather solely results from the interaction of the foil with the flow and its elastic supports (see Eq. 1). This “well-behaved” pitch motion has therefore been obtained passively.

Fig. 8a shows that the pitch amplitude increases with an increase of the dimensionless static moment (S^*) in the green regime. This behavior will be explained further below. Regarding the phase lag between the heave and the pitch motions, it is found to remain relatively close to 90° for all the operating points in this regime. More specifically, it ranges between approximately 90° and 105° . Regarding the efficiency, it increases as S^* increases (see Fig. 7) and the largest efficiencies are observed for the operating points with the largest dimensionless static moment values reached in this regime. These best efficiency points are obtained with intermediate prescribed frequencies.

More precisely, a maximum efficiency of 45.4% is achieved when $f^* = 0.20$ and $S^* = 0.65$. This is comparable to the best efficiencies reported for the fully-constrained turbine technology (Kinsey and Dumas, 2014; Xiao and Zhu, 2014), therefore confirming the great potential of this semi-passive turbine concept with a prescribed heave motion and a passive pitch motion. In the parametric study conducted by Kinsey and Dumas (2014) on the fully-constrained turbine, a maximum efficiency of 43.3% was obtained by respectively prescribing the reduced frequency, the pitch amplitude and the phase lag values to 0.18, 80° and 90° to a foil having its pitch axis located at the third-chord point ($x_p/c = 1/3$). In this study, for which $x_p/c = 1/4$, the best operating point has a pitch amplitude of 84.7° , a phase lag of 95.4° , and it has been passively obtained with a prescribed reduced frequency of 0.20.

The efficiency alone is not sufficient to fully characterize the performance of a flapping-foil turbine because it does not allow directly comparing the amount of power extracted by two operating points with different overall extents of the foil motion (d). The time-averaged power coefficient at the generator ($\overline{C_{P_{\text{gen}}}}$) is useful in that respect since it

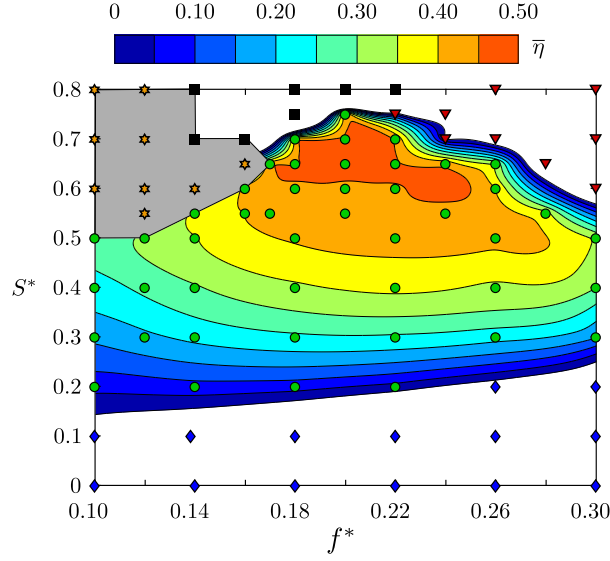


Figure 7: Contours of the time-averaged efficiency. A maximum efficiency of 45.4% is obtained when $f^* = 0.20$ and $S^* = 0.65$. The white areas indicate negative values.

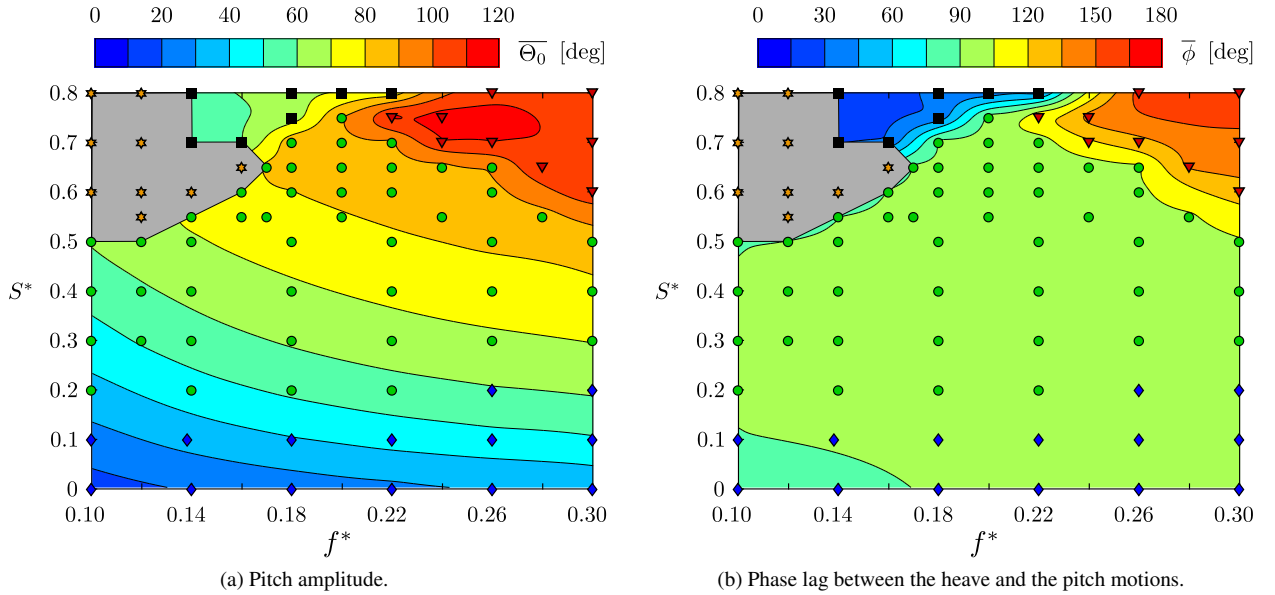


Figure 8: Contours of the time-averaged values of two metrics characterizing the foil motions.

normalizes the power with a common length scale, namely the chord length, instead of the overall extent of the foil motion in heave (d), which varies from an operating point to another. Contours of this metric are presented in Fig. 11.

Recalling that the heave amplitude (H_0) is constrained to one chord length for all the cases investigated in this work, the differences between the values of d for the various simulated operating points is solely due to the differences in pitch amplitude. The variations of d therefore remain relatively small between the different operating points in the energy-extraction regime with a minimum value of 2.15, when $f^* = 0.10$ and $S^* = 0.20$, and a maximum value of 2.71, when $f^* = 0.18$ and $S^* = 0.70$. Consequently, the topology is similar for the contours of the time-averaged efficiency ($\bar{\eta}$) and the time-averaged power coefficient at the generator ($\overline{C_{P_{\text{gen}}}}$). The maximum $\overline{C_{P_{\text{gen}}}}$ of 1.21 is not

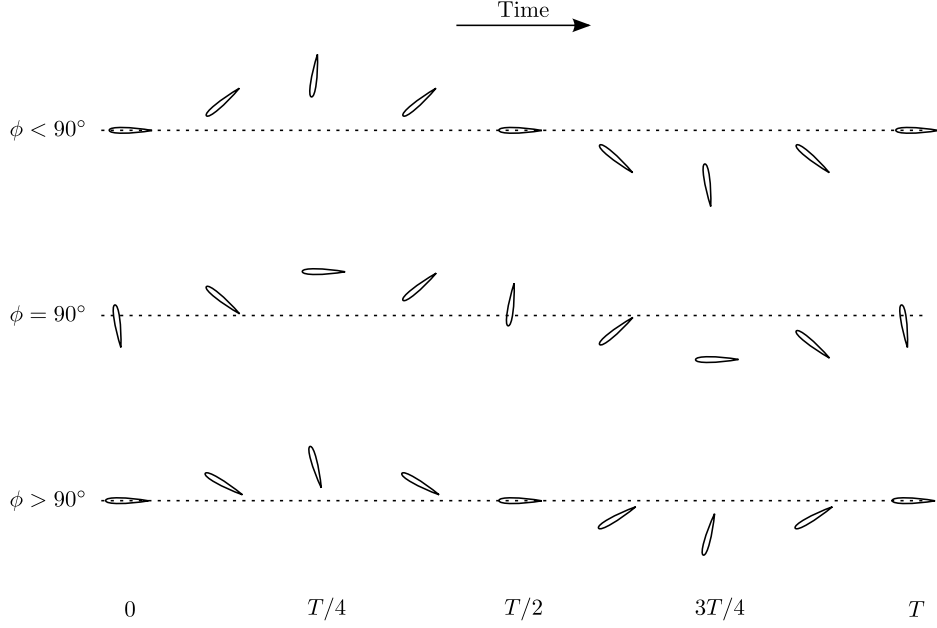


Figure 9: Typical foil motions as a function of time for different phase lag values between the heave and the pitch motions. The dashed line indicates the equilibrium position in heave ($h = 0$).

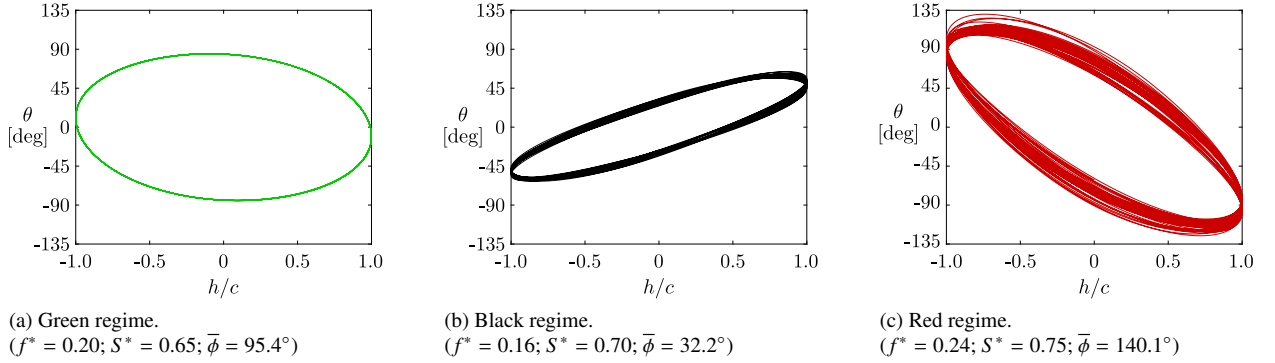


Figure 10: Limit-cycle oscillations for three of the five different regimes of motion. The motions follow counterclockwise trajectories.

observed at the maximum efficiency point but rather when $f^* = 0.20$ and $S^* = 0.75$. Nonetheless, this operating point is very close to the maximum efficiency point and the value of $\overline{C_{P_{\text{gen}}}}$ at the maximum efficiency point is very close to the maximum $\overline{C_{P_{\text{gen}}}}$, with a value of 1.19.

One can notice that a positive static moment is required in order to obtain the high efficiencies reported above. This means that the center of mass has to be located downstream of the pitch axis (see Eq. 2 and Fig. 1). In order to understand why this is needed, it is insightful to analyze the heave and pitch contributions to the time-averaged power coefficient at the generator ($\overline{C_{P_{\text{gen}}}}$), namely $\overline{C_{P_h}}$ and $\overline{C_{P_\theta}}$. As described in Sec. 2.3, the power coefficient at the generator is equal to the sum of the heave and pitch contributions when the motions are periodic (see Eq. 30), which is the case for all the simulated operating points in the energy-extraction regime. These two contributions are shown in Fig. 12.

It is found that the time-averaged pitch power coefficient ($\overline{C_{P_\theta}}$) is negative for all the operating points considered in this study. This indicates that the pitch motion never extracts energy from the flow in the mean but rather provides energy to the flow, hence acting as an energy sink in Eq. 16. This in turn means that when an operating point has a

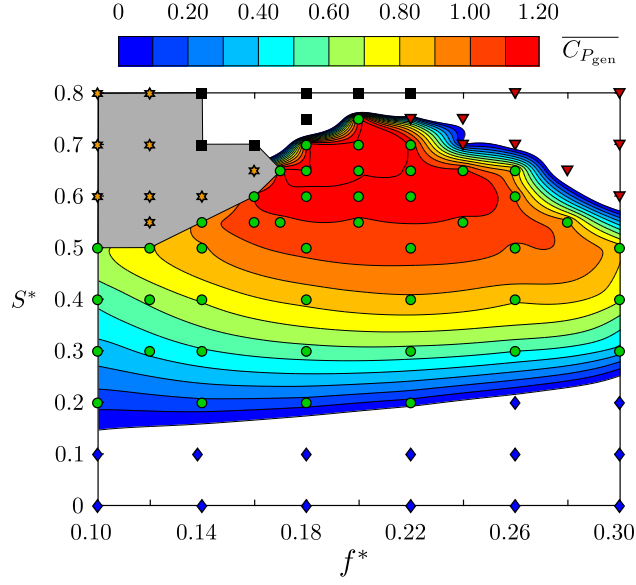


Figure 11: Contours of the time-averaged power coefficient available at the generator. The white areas indicate negative values.

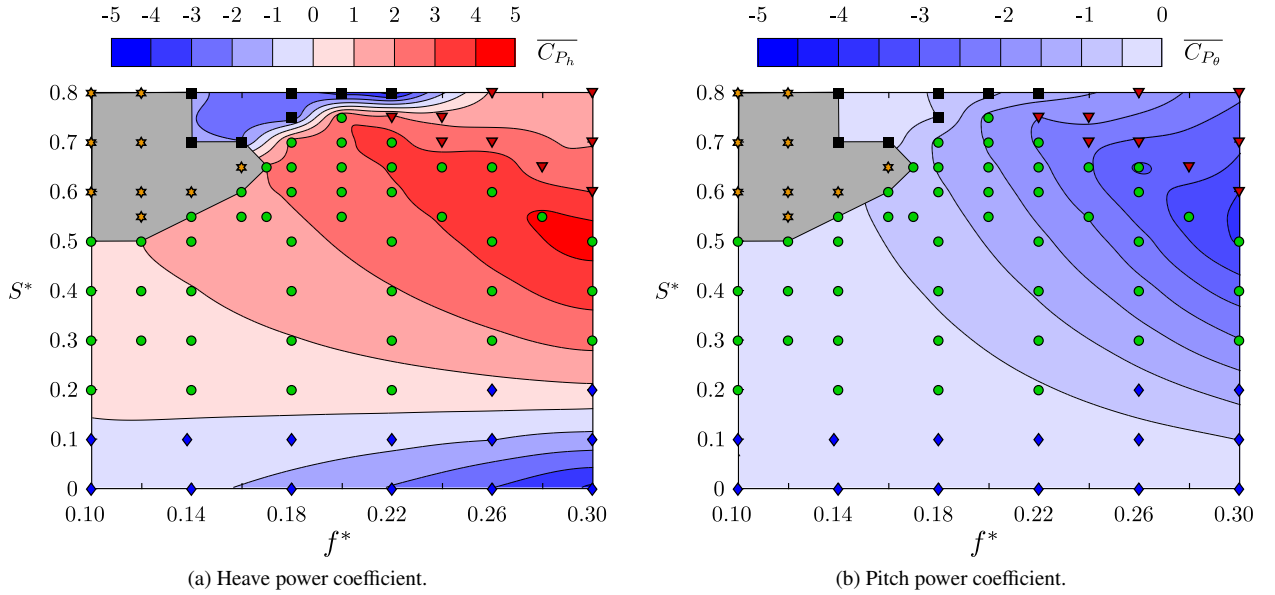


Figure 12: Contours of the time-averaged heave and pitch power coefficients.

positive efficiency, it must come from the heave contribution. Indeed, the time-averaged heave power coefficient ($\overline{C_{P_h}}$) is positive throughout the green regime.

Since D_θ^* has been set to zero and because the motions are periodic in the energy-extraction regime, Eq. 16 simplifies to Eq. 28. This indicates that the power transfer from the foil pitch motion to the flow ($\overline{C_{P_\theta}}$) can only be balanced by the power transfer from the heave motion to the pitch motion through the inertial coupling term involving the static moment ($\overline{C_{P_{S,\theta}}}$). In other words, $\overline{C_{P_{S,\theta}}}$ must be positive to balance the negative value of $\overline{C_{P_\theta}}$. Considering the prescribed heave motions and the passive pitch motions that have been obtained in the energy-extraction regime, this can only happen if the static moment is positive, thus implying that the center of mass has to be located downstream

of the pitch axis. It is also worth mentioning that Eq. 28 implies that when $S^* = 0$, and thus $\overline{C_{P_{S,\theta}}} = 0$ (see Eq. 24), $\overline{C_{P_\theta}}$ must also be equal to zero.

$\overline{C_{P_\theta}}$ is also usually negative in the case of fully-constrained flapping-foil turbines with good levels of performance (Campobasso et al., 2013; Kinsey and Dumas, 2014; Kim et al., 2017). With the fully-constrained concept, a power transfer from the foil pitch motion to the flow ($\overline{C_{P_\theta}} < 0$) can either be balanced by the presence of some rigid links that mechanically couple both degrees of freedom together, thereby allowing a transfer of power from the heave motion to the pitch motion to take place, or by the presence of an actuator in pitch, which would provide the necessary power. However, neither of these two possibilities is relevant in the case of the semi-passive turbine concept investigated in this work, thus leaving the static moment contribution as the sole mechanism to achieve a power balance for the pitch motion when $\overline{C_{P_\theta}}$ is negative.

It is still possible to extract energy from the flow with a positive value of $\overline{C_{P_\theta}}$. This is the case, for example, for the optimal operating point reported by Veilleux and Dumas (2017) with a fully-passive flapping-foil turbine having an efficiency of 29.1%. Under such circumstances, no transfer of power from the heave motion to the pitch motion is required. As a result, the dimensionless static moment can be equal to zero or even be negative. In fact, the optimal operating point found by Veilleux and Dumas (2017) had a dimensionless static moment of -0.029 . Consequently, some of the power extracted via the pitch motion was transferred from the pitch motion to the heave motion through the inertial coupling terms, but most of it was dissipated due to the presence of viscous friction in pitch. Veilleux and Dumas (2017) showed that the positive value of $\overline{C_{P_\theta}}$ was attributed to the formation of leading-edge vortices (LEVs) and their interaction with the foil motions. Indeed, the suction associated to the presence of LEVs was found to generate a moment about the pitch axis in the same direction as the pitch velocity, hence positively contributing to $\overline{C_{P_\theta}}$. The same observation was made by Zhu and Peng (2009) for a semi-passive flapping-foil turbine with a passive heave motion and a prescribed pitch motion. Conversely, Kinsey and Dumas (2014) showed that $\overline{C_{P_\theta}}$ was always negative when no LEVs were formed for a fully-constrained flapping-foil turbine undergoing sinusoidal heave and pitch motions. In the literature, the presence of LEVs has been widely recognized as being responsible for an enhanced performance (Young et al., 2014; Xiao and Zhu, 2014). However, most of the studies that led to this conclusion were conducted at low Reynolds numbers of the order of 1 000. At a much larger Reynolds number of 500 000, Kinsey and Dumas (2014) showed that the best efficiencies were rather obtained without LEVs. Indeed, they obtained a maximum efficiency of 43.3% without LEVs and a maximum efficiency of 35.1% with LEVs. This suggests that LEVs should be avoided at large Reynolds numbers to maximize the energy extraction. Negative values of $\overline{C_{P_\theta}}$ are therefore expected, which means that positive values of static moment are required.

In the present work, no leading-edge vortices are observed for any of the operating points in the energy-extraction regime. For example, the time evolution of the vorticity field for the best efficiency point is presented in Fig. 13. Moreover, the passive pitch motions are always very similar to sine waves in this regime. The present study therefore demonstrates that it is possible to passively obtain a pitch motion that is very close to the prescribed pitch motion characterizing the best fully-constrained flapping-foil turbine case reported by Kinsey and Dumas (2014) by adequately positioning the center of mass downstream of the pitch axis ($S^* > 0$) in order to provide the power required by the pitch motion ($\overline{C_{P_\theta}} < 0$). It should thus not be surprising to observe that the semi-passive and the fully-constrained flapping-foil turbines can achieve similar efficiencies.

The balance between the power transferred from the heave motion to the pitch motion ($\overline{C_{P_{S,\theta}}}$) and the power transferred to the flow via the foil pitch motion ($\overline{C_{P_\theta}}$) explains why the pitch amplitude increases with the dimensionless static moment (see Fig. 8a). Since the pitch motions are always similar to sine waves with relatively large amplitudes, the terms $\dot{\theta}$ and $\dot{\theta} \cos(\theta)$, which respectively appear in the definitions of $\overline{C_{P_\theta}}$ and $\overline{C_{P_{S,\theta}}}$, are both roughly proportional to the pitch amplitude. Considering that the phase lag remains relatively constant throughout the energy-extraction regime, this means that an increase of the dimensionless static moment or the amplitude of the heave acceleration (\ddot{h}) has to be balanced by an increase of the amplitude of the moment (M) generated by the fluid flow (see Eqs. 22 and 24). In this context and for a given prescribed frequency (f^*), and thus a given heave motion, the amplitude of M can only increase if the pitch amplitude increases. Consequently, an increase of S^* results in an increase of $\overline{C_{P_{S,\theta}}}$ and therefore allows for more negative values of $\overline{C_{P_\theta}}$ to occur, which in turn happens when the pitch amplitude increases.

$\overline{C_{P_{S,\theta}}}$ also increases with the reduced frequency (f^*) because \ddot{h} is proportional to the square of the frequency. The amplitude of M therefore also has to increase with f^* to respect the balance between $\overline{C_{P_{S,\theta}}}$ and $\overline{C_{P_\theta}}$. Such an increase of the moment with the reduced frequency would occur even if the pitch amplitude would remain constant due to

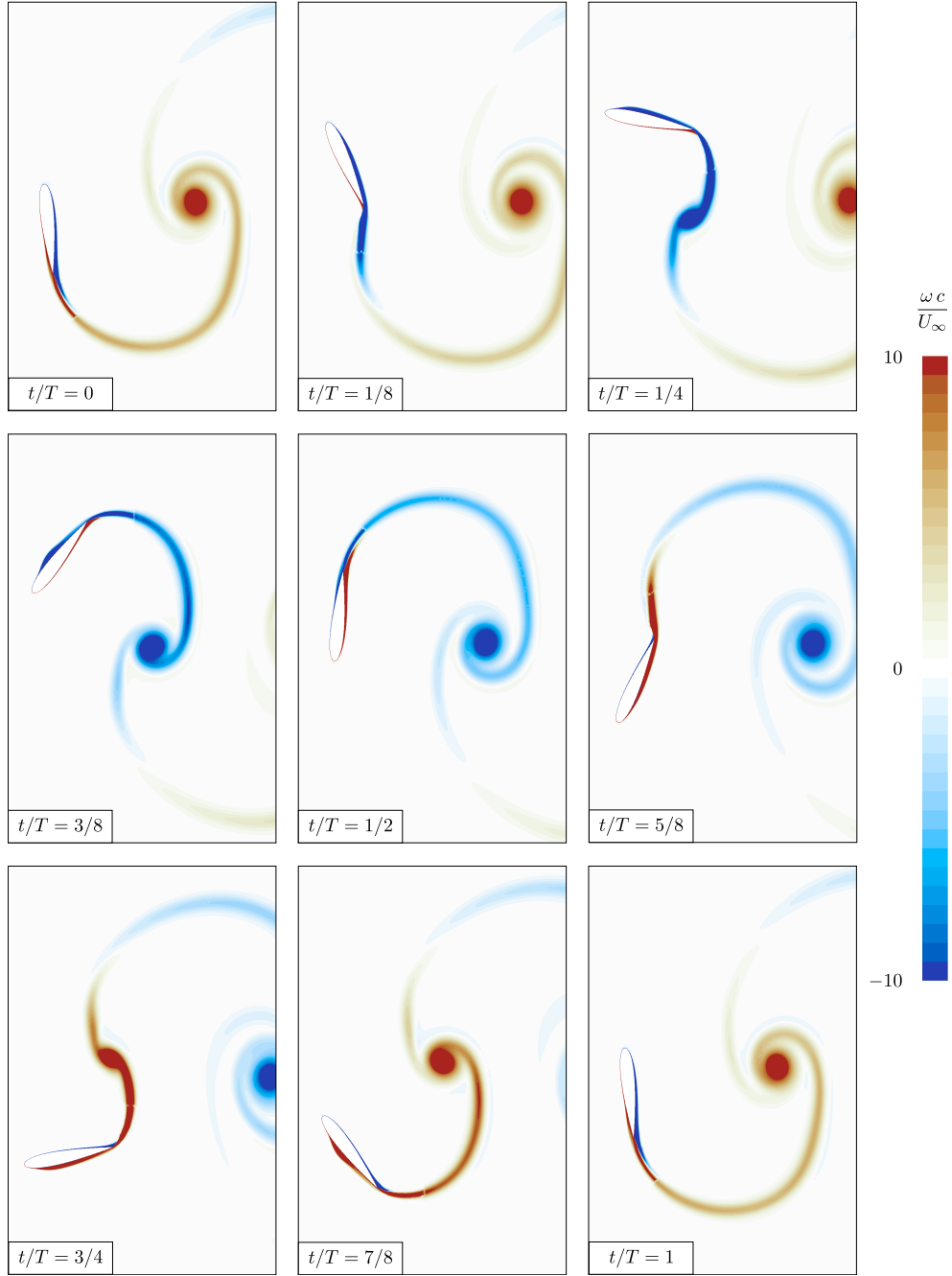


Figure 13: Time evolution of the dimensionless vorticity field ($\omega c/U_\infty$) during one cycle of the semi-passive turbine operating at its best efficiency point ($f^* = 0.20$ and $S^* = 0.65$).

larger pitch and heave velocities in the foil reference frame for larger f^* . Nevertheless, the pitch amplitude is still found to increase with f^* .

The time-averaged heave power coefficient also increases with the reduced frequency, as observed in Fig. 12a. The fact that it becomes more positive while C_{P_θ} becomes more negative as the frequency is increased results in a power coefficient at the generator and an efficiency that are less sensitive to the reduced frequency than $\overline{C_{P_h}}$ and $\overline{C_{P_\theta}}$, as long as we remain in the energy-extraction regime.

3.1.2. Blue regime (propulsion)

The motions in the blue regime (operating points denoted with blue diamonds) are similar to those in the green regime. Indeed, they are periodic (see Fig. 6b), no LEVs are formed and the phase lag between the heave and the pitch motions is still around 90° , ranging between 80° and 100° , as observed in Fig. 8b. The main difference between these two regimes is the pitch amplitude. More specifically, Fig. 8a shows that the pitch amplitude continues to decrease when switching from the green regime to the blue regime as the dimensionless static moment decreases down to zero. The consequence is that the energy-extraction regime switches to a propulsion regime. Indeed, Fig. 14 presents the contours of the time-averaged streamwise force coefficient ($\overline{C_{F_x}}$) and shows that all the operating points are characterized by a positive streamwise force coefficient ($\overline{C_{F_x}} > 0$) except for most of the operating points in the blue regime, which rather have a negative streamwise coefficient ($\overline{C_{F_x}} < 0$) or, in other words, a positive thrust coefficient. Consequently, these operating points require energy on a time-averaged basis instead of generating some ($\overline{\eta} < 0$ in Fig. 7). The cases with $f^* = 0.26$ and $S^* = 0.20$ and with $f^* = 0.30$ and $S^* = 0.20$ are two exceptions for which the streamwise force coefficient is positive, but the efficiency is negative.

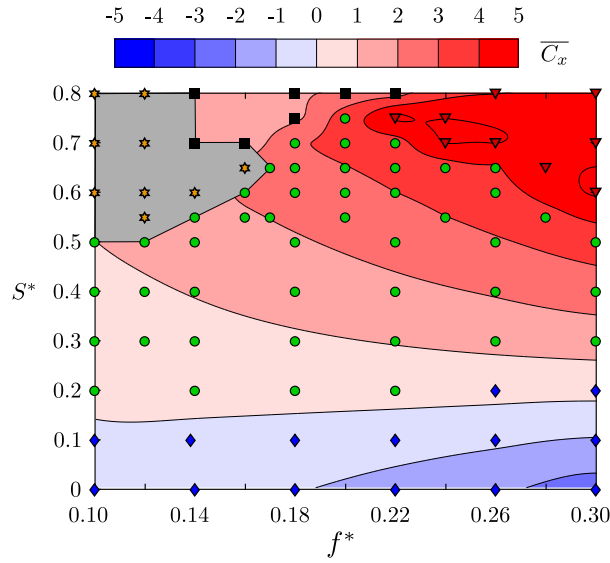


Figure 14: Contours of the time-averaged streamwise force coefficient.

Since the motions in the blue regime are periodic like in the green regime, the power coefficient at the generator can still be expressed as the sum of the heave and pitch power coefficients (see Eq. 30). As mentioned in the previous section, the time-averaged pitch power coefficient ($\overline{C_{P_\theta}}$) is negative throughout the current parametric study, thereby leaving the time-averaged heave power coefficient ($\overline{C_{P_h}}$) as the sole possible contributor to a positive energy extraction. In fact, it is found that $\overline{C_{P_h}}$ changes sign between the green and the blue regimes. This is attributed to a change of sign of the heave force resulting from a change of sign of the effective angle of attack as the pitch amplitude decreases below a specific threshold, which depends on the frequency of the motions (Kinsey and Dumas, 2008). For example, time evolutions of the heave power coefficient (C_{P_h}), the dimensionless heave velocity (\dot{h}^*) and the heave force coefficient (C_{F_y}) are shown over one cycle for an operating point in the green regime and another one in the blue regime in Fig. 15. Note that the heave power coefficient can be expressed as the product of the heave force coefficient with the dimensionless heave velocity. This figure shows that the heave force coefficient is in phase with the dimensionless heave velocity in the green regime (see Fig. 15a), while the two are about 180° out of phase in the blue regime (see Fig. 15b) due to a change of sign of C_{F_y} . More information on the relation between the pitch amplitude and the transition between an energy-extraction regime and a propulsion regime is given in the works of Xiao and Zhu (2014) and Kinsey and Dumas (2008).

Lastly, it is worth noting that Mackowski and Williamson (2017) used their cyber-physical facility to study a flapping foil with a prescribed pitch motion and a passive heave motion and they obtained their best propulsion performances with the center of mass upstream of the pitch axis, i.e., a negative static moment.

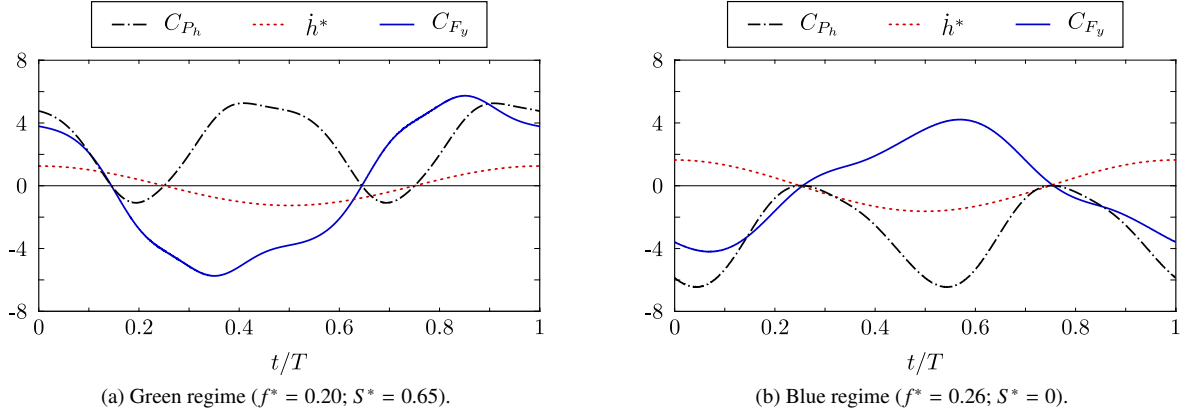


Figure 15: Time evolutions of the heave power coefficient (C_{P_h}), the dimensionless heave velocity (h^*) and the heave force coefficient (C_{F_y}) over one cycle for an operating point in the green regime and another one in the blue regime. The instant $t/T = 0$ corresponds to a moment at which $h = 0$ and $\dot{h} > 0$.

3.1.3. Black regime

The black regime (operating points denoted with black squares) is significantly different. During the initial transient period, the operating points in this regime behave like those in the green regime. The phase lag is initially around 90° and the pitch amplitude grows from cycles to cycles. For the operating points in the green regime, Fig. 16a shows that the moment coefficient generated by the flow about the pitch axis (C_M) is negative and maximum (in absolute value) when the maximum positive pitch velocity is reached, i.e., when the foil is at its maximum (positive) position in heave and $\theta = 0$, considering a phase lag of 90° . The opposite occurs around the minimum (negative) heave position.

Fig. 16b shows that this behavior is also observed for the operating points in the black regime at the beginning of the simulations. However, as the pitch amplitude keeps growing, the boundary layers eventually separate near the leading edge and large leading-edge vortices are formed and alter the hydrodynamic moment about the pitch axis, as shown in Fig. 17. They are formed before the instant at which the maximum pitch velocity is reached and they have the time to travel past the pitch axis before this specific instant due to the relatively low reduced frequency characterizing the operating points in this regime. As a result, the suction associated to the LEVs generates a positive contribution to the moment about the pitch axis when the pitch velocity is positive and maximum, and vice versa. For instance, the LEV that is observed at the instant $t/T = 5.83$ in Fig. 17a generates a negative contribution to the moment about the pitch axis when the pitch velocity is negative, as seen in Fig. 17b.

As already mentioned, the same phenomenon was also observed by Veilleux and Dumas (2017) and Zhu and Peng (2009). This modification of the hydrodynamic moment about the pitch axis then alters the phase lag and the pitch amplitude, which both quickly drop to smaller values for the subsequent foil oscillations. Following this series of events, a new limit-cycle oscillation regime is reached, which is characterized by moderate pitch amplitudes, phase lag values below 90° and the formation of LEVs. The occurrence of the boundary layers separation and the associated formation of LEVs are responsible for the slight variations observed for the efficiency, pitch amplitude and phase lag values from cycles to cycles (e.g., see Figs. 6c and 10b). Lastly, none of the operating points in the black regime extracts energy on a time-averaged basis.

3.1.4. Orange regime

Even though the time evolution of the pitch angle appears to be very different in the orange regime (operating points denoted with orange stars) than in the black regime (see Figs. 6c and 6d), these two regimes are actually very similar. Indeed, the series of events leading to a new limit-cycle oscillation regime that have been described in the previous section also happens in the case of the orange regime. Strong LEVs are formed and affect the moment about the pitch axis, as observed in Fig. 17. This results in sudden drops of the pitch amplitude and the phase lag between the heave and the pitch motions. The difference is that the drop in pitch amplitude is so important that the boundary layers eventually reattach. Following that, the foil starts to behave as in the transient period of the green regime again

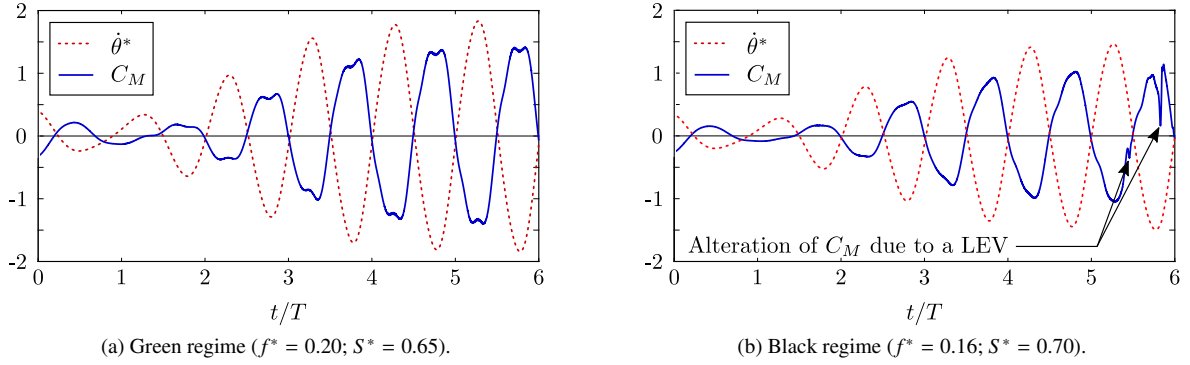
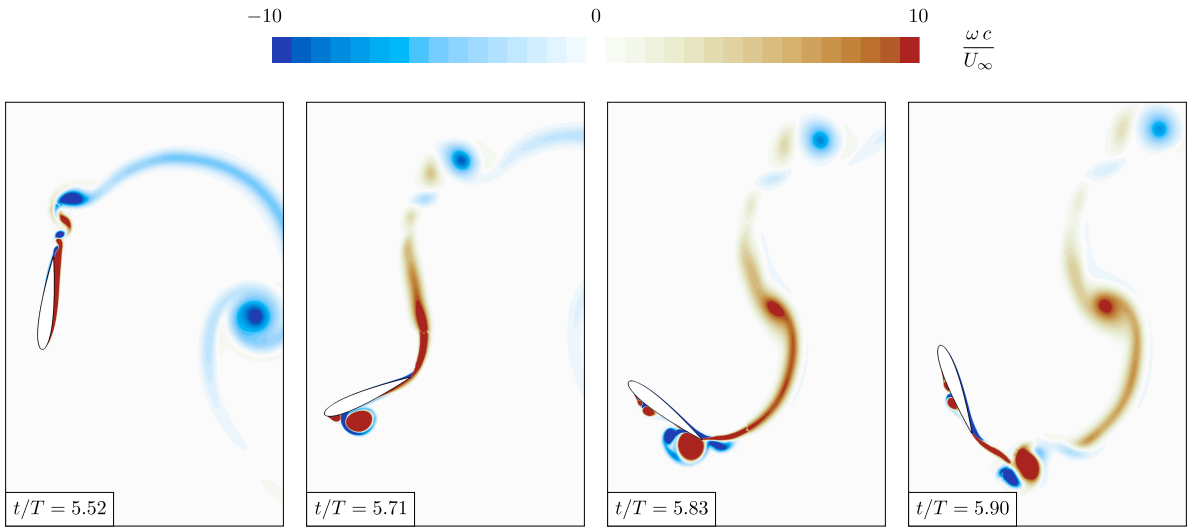
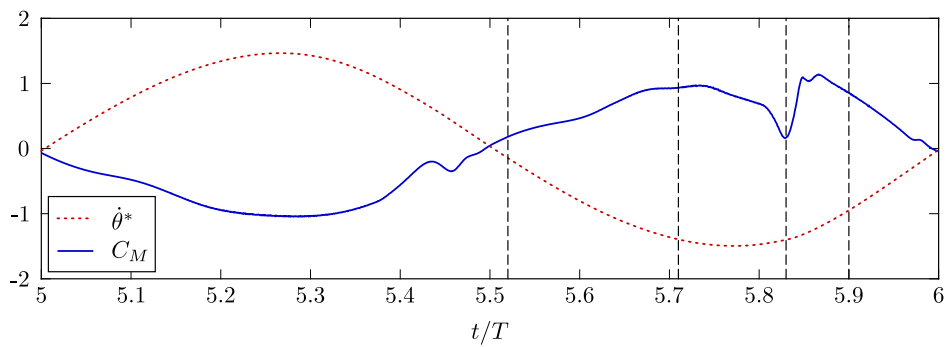


Figure 16: Time evolutions of the dimensionless pitch velocity ($\dot{\theta}^*$) and the moment coefficient (C_M) over the six first foil oscillations for an operating point in the green regime and another one in the black regime.



(a) Snapshots of the dimensionless vorticity field ($\omega c/U_\infty$) at some specific instants.



(b) Time evolutions of the dimensionless pitch velocity ($\dot{\theta}^*$) and the moment coefficient (C_M) during the 6th foil oscillation. The vertical dashed lines indicate the instant at which the different snapshots presented in Fig. 17a have been taken.

Figure 17: Influence of the formation of LEVs on the moment coefficient for a representative operating point in the black regime ($f^* = 0.16$ and $S^* = 0.70$). The instant $t/T = 0$ corresponds to the beginning of the simulation.

and the pitch amplitude restarts to grow until the boundary layers separate and LEVs are formed once more. This process is repeated endlessly.

Since the operating points in the orange regime alternate between the motion characteristics specific to the green and the black regimes, it is not surprising that the efficiency is found to oscillate between positive and negative values. Indeed, the efficiency can reach values as high as 40% for a few consecutive cycles and then quickly drop to values as low as -90% before becoming positive again. As mentioned earlier, such large variations make this regime inappropriate for a turbine application.

3.1.5. Red regime

The last regime, the red one (operating points denoted with red triangles), is also resulting from the formation of LEVs. The initial transient period is similar to the one in the green regime, like for the black and orange regimes. Again, the growth of the pitch amplitude eventually leads to the separation of the boundary layers near the leading edge and the formation of strong LEVs, which alter the moment generated by the fluid flow about the pitch axis. The first difference is that the formation of LEVs is delayed because the prescribed reduced frequencies are larger in this regime, hence resulting in smaller effective angles of attack for given pitch amplitudes (Kinsey and Dumas, 2014). The larger reduced frequencies also result in faster pitch motions with respect to the speed at which the LEVs travel downstream. Consequently, the LEVs do not have the time to travel past the pitch axis before the maximum pitch velocity is reached, unlike what happens for the black and orange regimes. Instead of generating a positive contribution to the moment about the pitch axis when the pitch velocity is positive and maximum, the LEVs rather result in a negative moment contribution. This strong dependence of the moment coefficient to the time at which the LEVs travel past the pitch axis location as already been pointed out by Young et al. (2013, 2014). The outcome in the case of the operating points in the red regime is that the growth of the pitch amplitude is extended and the phase lag increases and exceeds 90° until a permanent limit-cycle oscillation regime is finally reached. More than 50 complete foil oscillations can be needed before reaching these limit-cycle oscillations, which is much more than for all the other regimes of motion presented in the previous sections. Strong LEVs are still formed during this permanent response, which results in variations of the efficiency, the pitch amplitude and the phase lag from cycles to cycles. Furthermore, the wake is not convected as fast with respect to the foil motions in the red regime than in the black regime due to the fact that the reduced frequencies are larger. The stronger interaction occurring between the flapping foil and its wake in the red regime results in larger variations of the motions from cycles to cycles than in the black regime.

The difference between the black and the red regimes is subtle as it is only related to a different timing between the pitch motion and the formation and convection of LEVs. The operating point characterized with $f^* = 0.22$ and $S^* = 0.80$ has even behaved like the operating points in the red regime during the first 50 cycles before finally switching to a limit-cycle oscillation regime characterizing the black regime.

Lastly, a summary of the characteristics of each regime is given in Table 3.

Table 3: Summary of the characteristics describing each regime of motion.

Regime	$\bar{\eta}$	$\bar{\Theta}_0$	$\bar{\phi}$
Green	> 0	40° to 90°	90° to 105°
Blue	< 0	15° to 60°	80° to 100°
Black	< 0	55° to 70°	30° to 40°
Orange	Alternate between the green and black regimes		
Red	< 0	105° to 110°	115° to 155°

3.1.6. Boundaries between the different regimes of motion

One can notice that some of the best operating points lie on the edge of the energy-extraction regime (see Fig. 7). This means that a small change in the operating conditions of these points could lead to a considerable drop in performance. For example, such a consequence could happen if the freestream flow was perturbed, hence affecting the reduced frequency. The reason for this very abrupt drop in performance is due to the sudden nature of separation.

As mentioned before, no leading-edge vortices (LEVs) are observed in this study for all the operating points in the energy-extraction regime. Conversely, LEVs are formed for all the operating points in the black, the orange and the red regimes. Extra care should therefore be taken when selecting an operating point since the exact position of the boundaries between the green regime and the black, orange and red regimes is expected to be sensitive to the specific characteristics of a given flow. More specifically, every aspect of the flow that can affect the robustness of the boundary layers, such as the Reynolds number and the turbulence level in the freestream flow, for example, is expected to affect the locations of these boundaries. On the other hand, the performances achieved by the operating points in the green regime are not expected to be significantly affected by these aspects.

This sensitivity of the semi-passive turbine performance to the occurrence of separation is more pronounced than in the case of the fully-constrained turbine concept. A decrease of performance has also been reported for such turbines when LEVs are formed, but not a sharp drop (Kinsey and Dumas, 2014). This is because the forces acting on the foil are affected by the LEVs, but not the motions since they are prescribed rather than being passive. In the case of the semi-passive turbine studied in the current work, not only the forces are affected, but also the motions.

3.2. Role of the electric generator

It is evident that the operating points requiring energy on a time-averaged basis to sustain the foil motions ($\bar{\eta} < 0$) require the electric generator to act as an actuator. However, the operating points in the energy-extraction regime can also require that the electric generator acts as an actuator at some instants during the foil oscillations. In other words, this means that even though the power coefficient at the generator is positive on a cycle-averaged basis ($\langle C_{P_{\text{gen}}} \rangle > 0$), it can become negative at some instants during one cycle. In order to explain this point, an instantaneous version of Eq. 15 is analyzed:

$$C_{P_h} + C_{P_{m_h}} + C_{P_{S,h}} + C_{P_{D_h}} = C_{P_{\text{gen}}} . \quad (38)$$

If no friction is considered in heave, $D_h = 0$ and thus $C_{P_{D_h}} = 0$. However, $C_{P_{m_h}}$ has to be considered since it only becomes equal to zero on a cycle-averaged basis⁴. The best efficiency point ($f^* = 0.20$ and $S^* = 0.65$) is selected for the analysis and an arbitrary value of 1 is considered for m_h . The resulting values of $C_{P_{m_h}}$ along with the values of the other terms appearing in Eq. 38 are shown over one cycle in Fig. 18. The term $C_{P_{D_h}}$ is not shown since it is equal to zero and the terms C_{P_h} and $C_{P_{S,h}}$ are combined together.

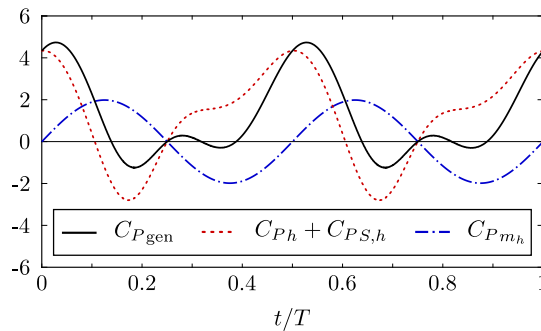


Figure 18: Time evolutions of the instantaneous power coefficient at the generator ($C_{P_{\text{gen}}}$) and its contributions (see Eq. 38) over one cycle of the best efficiency point ($f^* = 0.20$ and $S^* = 0.65$). No friction is considered in heave ($D_h = 0$) and an arbitrary value of 1 is considered for m_h .

This figure shows that the term $C_{P_{m_h}}$ oscillates between positive and negative values with a cycle-averaged value of zero, as expected. This means that the value of m_h does not affect the cycle-averaged power coefficient at the

⁴Considering that the heave motion is periodic

generator, but it affects its instantaneous value. In order to avoid requiring to use the electric generator as an actuator, $C_{P_{\text{gen}}}$ would need to remain positive throughout the cycle. However, it is found to be negative at different instants when $m_h = 1$. Since this happens both at moments when $C_{P_{m_h}}$ is positive and negative, there is no value of m_h that would allow $C_{P_{\text{gen}}}$ to always remain positive. Nevertheless, this is not problematic because a typical electric generator can act as an actuator. Indeed, fully-constrained flapping-foil turbines also require the electric generator to act as an actuator at some instants during the foil oscillations, such as in the case of the prototype that has been designed and tested by Kinsey et al. (2011).

The semi-passive turbine concept proposed in this study also requires some power to reach the limit-cycle oscillations that characterize the energy-extraction regime. Indeed, the pitch amplitude starts from zero and has to pass through small pitch amplitudes that characterize the propulsion regime (blue regime) before reaching the larger pitch amplitudes characterizing the energy-extraction regime (green regime). This means that the semi-passive turbine concept is not self-starting.

4. Conclusion

Two-dimensional URANS simulations have been conducted to investigate the potential of a novel semi-passive flapping-foil turbine with a prescribed heave motion and a passive pitch motion. Throughout the parametric study, the Reynolds number has been set to 3.9×10^6 based on the chord length, the pitch axis has been located at the quarter-chord point ($x_p/c = 0.25$), the dimensionless heave amplitude (H_0/c), the dimensionless moment of inertia about the pitch axis (I_θ^*) and the dimensionless pitch damping coefficient (D_θ^*) have been respectively set to 1, 2 and 0, and the dimensionless pitch spring stiffness coefficient (k_θ^*) has been chosen so that the pitch natural frequency matches the frequency of the prescribed heave motion.

By varying the reduced frequency and the dimensionless static moment (S^*), five different regimes of motion have been observed based on the time-averaged efficiency ($\overline{\eta}$), pitch amplitude ($\overline{\Theta}_0$) and phase lag ($\overline{\phi}$) values as well as the regularity of the motions. Among these different responses, one corresponds to an energy-extraction regime and is characterized by periodic limit-cycle oscillations with large pitch amplitudes and no formation of LEVs. It has been shown that the center of mass needs to be located downstream of the pitch axis for such motions to occur in order to balance the power required to sustain the pitch motion with a transfer of power from the heave motion to the pitch motion via the inertial coupling terms in the equations of motion. In practice, this could be achieved with the use of an asymmetric flywheel having the required mass distribution.

A maximum efficiency of 45.4% has been obtained with a pitch amplitude of 84.7° and a phase lag of 95.4° when $f^* = 0.20$ and $S^* = 0.65$. This performance confirms the great potential of the heave-prescribed semi-passive flapping-foil turbine since this efficiency is of the same order as the best efficiencies reported for the fully-constrained flapping-foil turbine concept (Kinsey and Dumas, 2014; Xiao and Zhu, 2014), but it is obtained here with a simpler device in terms of the structural design.

Even though a considerable amount of energy can be extracted from the flow on a time-averaged basis, the electric generator needs to act as an actuator at some instants during the foil oscillations when limit-cycle oscillations are reached as well as to start the device.

Finally, it is worth mentioning that several important structural parameters (see Table 1) have not been varied in this first investigation of the semi-passive flapping-foil turbine concept with a prescribed heave motion and a passive pitch motion. Future works are therefore needed in that regard.

Acknowledgments

Financial support from the Natural Sciences and Engineering Research Council of Canada (NSERC Discovery Grant/RGPIN/121819-2013 and CGS-D scholarship), the Tyler Lewis Clean Energy Research Foundation (2016 TL-CERF grant) and the Leadership and Sustainable Development Scholarship Program of Université Laval is gratefully acknowledged by the authors. The computations presented in this work have been carried out on the supercomputer Colosse at Université Laval, managed by Calcul Québec and Compute Canada.

Appendix A. Fluid-solid coupling algorithm in pseudocode

Beginning of the n^{th} time step

1. Computation of the prescribed heave position, velocity and acceleration at the current time step ($h^n, \dot{h}^n, \ddot{h}^n$);
2. Execution of the solid solver for the i^{th} outer loop:

IF $i = 1$ (first outer loop) **THEN**

- a. Initial guess for the pitch angle at the current time step (θ^n) using the explicit second-order Adams-Bashforth scheme:

$$\theta_1^n = \theta^{n-1} + \frac{\Delta t}{2} (3\dot{\theta}^{n-1} - \dot{\theta}^{n-2}) ; \quad (\text{A.1})$$

ELSE IF $i = 2$ (second outer loop) **THEN**

- a. Initial guess for the Jacobian:

$$J_2^n = J^{n-1} ; \quad (\text{A.2})$$

- b. Computation of the new pitch angle:

$$\theta_2^n = \theta_1^n - \frac{R_{\theta_1}^n}{J_2^n} ; \quad (\text{A.3})$$

ELSE IF $i > 2$ (subsequent outer loops) **THEN**

- a. Computation of the Jacobian:

$$J_i^n = \frac{R_{\theta_{i-1}}^n - R_{\theta_{i-2}}^n}{\theta_{i-1}^n - \theta_{i-2}^n} ; \quad (\text{A.4})$$

- b. Computation of the new pitch angle:

$$\theta_i^n = \theta_{i-1}^n - \frac{R_{\theta_{i-1}}^n}{J_i^n} ; \quad (\text{A.5})$$

END IF

3. Foil rotation according to the updated pitch angle (θ_i^n);
4. Check if the solid convergence criterion is met:

IF $\left(\frac{|\theta_i^n - \theta_{i-1}^n|}{\pi/2} < \epsilon \text{ AND } i > 2 \right)$ **THEN**

- a. Execution of the fluid solver: perform fluid iterations until the fluid residuals convergence criteria are met;
- b. Incrementation of the time step and return to step 1.

ELSE THEN

- a. Execution of the fluid solver: perform fluid iterations until the value of the moment with the updated pitch angle (M_i^n) is converged;
- b. Computation of $\dot{\theta}_i^n$ and $\ddot{\theta}_i^n$ using the updated pitch angle θ_i^n with Eqs. 9 and 10;
- c. Computation of the residual:

$$R_{\theta_i}^n = I_{\theta} \ddot{\theta}_i^n + S \dot{h}^n \cos(\theta_i^n) + D_{\theta} \dot{\theta}_i^n + k_{\theta} \theta_i^n - M_i^n ; \quad (\text{A.6})$$

- d. Incrementation of the outer loop and return to step 2.

END IF

References

- Abiru, H., Yoshitake, A., 2011. Study on a Flapping Wing Hydroelectric Power Generation System. *Journal of Environment and Engineering* 6 (1), 178–186.
- Abiru, H., Yoshitake, A., 2012. Experimental Study on a Cascade Flapping Wing Hydroelectric Power Generator. *Journal of Energy and Power Engineering* 6 (9), 1429–1436.
- Boudreau, M., Dumas, G., 2017. Comparison of the wake recovery of the axial-flow and cross-flow turbine concepts. *Journal of Wind Engineering and Industrial Aerodynamics* 165, 137 – 152.
- Boudreau, M., Dumas, G., Rahimpour, M., Oshkai, P., 2018. Experimental investigation of the energy extraction by a fully-passive flapping-foil hydrokinetic turbine prototype. *Journal of Fluids and Structures* 82, 446 – 472.
- Campobasso, M. S., Piskopakis, A., Drofelnik, J., Jackson, A., 2013. Turbulent Navier-Stokes analysis of an oscillating wing in a power-extraction regime using the shear stress transport turbulence model. *Computers & Fluids* 88, 136 – 155.
- Cape Sharp Tidal Venture Ltd., 2018. <http://capesharptidal.com/>, accessed: 2018-10-09.
- Chen, Y., Nan, J., Wu, J., 2018. Wake effect on a semi-active flapping foil based energy harvester by a rotating foil. *Computers & Fluids* 160, 51 – 63.
- Dacles-Mariani, J., Kwak, D., Zilliac, G., 1999. On numerical errors and turbulence modeling in tip vortex flow prediction. *International Journal for Numerical Methods in Fluids* 30 (1), 65 – 82.
- Dacles-Mariani, J., Zilliac, G. G., Chow, J. S., Bradshaw, P., 1995. Numerical/Experimental Study of a Wingtip Vortex in the Near Field. *AIAA Journal* 33 (9), 1561 – 1568.
- Deng, J., Teng, L., Pan, D., Shao, X., 2015. Inertial effects of the semi-passive flapping foil on its energy extraction efficiency. *Physics of Fluids* 27 (5), 053103 (17 pp.) –.
- Derakhshandeh, J., Arjomandi, M., Dally, B., Cazzolato, B., 2016. Flow-induced vibration of an elastically mounted airfoil under the influence of the wake of a circular cylinder. *Experimental Thermal and Fluid Science* 74, 58 – 72.
- Ferziger, J., Perić, M., 2002. *Computational Methods for Fluid Dynamics*, 3rd Edition. Springer.
- Griffith, M. D., Jacono, D. L., Sheridan, J., Leontini, J. S., 2016. Passive heaving of elliptical cylinders with active pitching from cylinders towards flapping foils. *Journal of Fluids and Structures* 67, 124 – 141.
- Huxham, G. H., Cochard, S., Patterson, J., 2012. Experimental Parametric Investigation of an Oscillating Hydrofoil Tidal Stream Energy Converter. In: *Proceedings of the 18th Australasian Fluid Mechanics Conference*. Launceston, Australia.
- Kim, D., Strom, B., Mandre, S., Breuer, K., 2017. Energy harvesting performance and flow structure of an oscillating hydrofoil with finite span. *Journal of Fluids and Structures* 70, 314 – 326.
- Kinsey, T., Dumas, G., 2008. Parametric Study of an Oscillating Airfoil in a Power-Extraction Regime. *AIAA Journal* 46 (6), 1318–1330.
- Kinsey, T., Dumas, G., 2012. Computational Fluid Dynamics Analysis of a Hydrokinetic Turbine Based on Oscillating Hydrofoils. *Journal of Fluids Engineering* 134 (2), 021104 (16 pp.) –.
- Kinsey, T., Dumas, G., 2014. Optimal Operating Parameters for an Oscillating Foil Turbine at Reynolds Number 500,000. *AIAA Journal* 52 (9), 1885–1895.
- Kinsey, T., Dumas, G., Lalande, G., Ruel, J., Mehut, A., Viarouge, P., Lemay, J., Jean, Y., 2011. Prototype testing of a hydrokinetic turbine based on oscillating hydrofoils. *Renewable Energy* 36 (6), 1710 – 1718.
- Mackowski, A. W., Williamson, C. H. K., Jan 2017. Effect of pivot location and passive heave on propulsion from a pitching airfoil. *Phys. Rev. Fluids* 2, 013101.
- Peng, Z., Zhu, Q., 2009. Energy harvesting through flow-induced oscillations of a foil. *Physics of Fluids* 21 (12), 174–191.
- Shiels, D., Leonard, A., Roshko, A., 2001. Flow-induced vibration of a circular cylinder at limiting structural parameters. *Journal of Fluids and Structures* 15 (1), 3 – 21.
- Shimizu, E., Isogai, K., Obayashi, S., 2008. Multiobjective Design Study of a Flapping Wing Power Generator. *Journal of Fluids Engineering* 130 (2), 021104 (8 pp.) –.
- Sitorus, P. E., Ko, J. H., 2019. Power extraction performance of three types of flapping hydrofoils at a Reynolds number of 1.7E6. *Renewable Energy* 132, 106 – 118.
- Sitorus, P. E., Le, T. Q., Ko, J. H., Truong, T. Q., Park, H. C., 2015. Design, implementation, and power estimation of a lab-scale flapping-type turbine. *Journal of Marine Science and Technology*.
- Spalart, P. R., Allmaras, S. R., 1994. A One-Equation Turbulence Model for Aerodynamic Flows. *Recherche Aérospatiale* (1), 5–21.
- Spalart, P. R., Jou, W.-H., Strelets, M., Allmaras, S. R., 1997. Comments on the Feasibility of LES for Wings, and on a Hybrid RANS/LES Approach. In: *Advances in DNS/LES, Proceedings of the First AFOSR International Conference on DNS/LES*. Ruston, Louisiana, USA, pp. 137 – 147.
- Spalart, P. R., Rumsey, C. L., 2007. Effective inflow conditions for turbulence models in aerodynamic calculations. *AIAA Journal* 45 (10), 2544 – 2553.
- Teng, L., Deng, J., Pan, D., Shao, X., 2016. Effects of non-sinusoidal pitching motion on energy extraction performance of a semi-active flapping foil. *Renewable Energy* 85, 810 – 818.
- Veilleux, J.-C., 2014. Optimization of a Fully-Passive Flapping-Airfoil Turbine. Master's thesis, Université Laval, Québec, Québec, Canada.
- Veilleux, J.-C., Dumas, G., 2017. Numerical optimization of a fully-passive flapping-airfoil turbine. *Journal of Fluids and Structures* 70, 102 – 130.
- Wang, Z., Du, L., Zhao, J., Sun, X., 2017. Structural response and energy extraction of a fully passive flapping foil. *Journal of Fluids and Structures* 72, 96 – 113.
- Wu, J., Chen, Y. L., Zhao, N., 2015. Role of induced vortex interaction in a semi-active flapping foil based energy harvester. *Physics of Fluids* 27 (9), 093601.
- Wu, J., Qiu, Y. L., Shu, C., Zhao, N., 2014. Pitching-motion-activated flapping foil near solid walls for power extraction: A numerical investigation. *Physics of Fluids* 26 (8), 083601.
- Xiao, Q., Zhu, Q., 2014. A review on flow energy harvesters based on flapping foils. *Journal of Fluids and Structures* 46, 174–191.

- Young, J., Ashraf, M. A., Lai, J. C. S., Platzer, M. F., 2013. Numerical Simulation of Fully Passive Flapping Foil Power Generation. *AIAA Journal* 51 (11), 2727–2739.
- Young, J., Lai, J. C. S., Platzer, M. F., 2014. A review of progress and challenges in flapping foil power generation. *Progress in Aerospace Sciences* 67, 2–28.
- Zhan, J., Xu, B., Wu, J., Wu, J., 2017. Power extraction performance of a semi-activated flapping foil in gusty flow. *Journal of Bionic Engineering* 14 (1), 99 – 110.
- Zhu, Q., 5 2011. Optimal frequency for flow energy harvesting of a flapping foil. *Journal of Fluid Mechanics* 675, 495–517.
- Zhu, Q., 2012. Energy harvesting by a purely passive flapping foil from shear flows. *Journal of Fluids and Structures* 34, 157–169.
- Zhu, Q., Haase, M., Wu, C. H., 2009. Modeling the capacity of a novel flow-energy harvester. *Applied Mathematical Modelling* 33 (5), 2207–2217.
- Zhu, Q., Peng, Z., 2009. Mode coupling and flow energy harvesting by a flapping foil. *Physics of Fluids* 21 (3), 033601 (10 pp.) –.